
NEURAL INFORMATION FIELD FILTER

A PREPRINT

 **Kairui Hao***

School of Mechanical Engineering
Purdue University
West Lafayette, IN
hao55@purdue.edu

 **Ilias Bilionis**

School of Mechanical Engineering
Purdue University
West Lafayette, IN
ibilion@purdue.edu

July 24, 2024

ABSTRACT

We introduce neural information field filter, a generic Bayesian state and parameter estimation method for high-dimensional nonlinear dynamical systems given large measurement datasets. Solving such a problem using traditional methods, such as Kalman and particle filters, is exceptionally computationally expensive. Information field theory is a Bayesian approach that can computationally efficiently reconstruct dynamical model state paths and calibrate model parameters from noisy measurement data. To apply the method, we first parameterize the time evolution state path using the span of a finite linear basis. The existing method has to reparameterize the state path by initial states to satisfy the initial condition. Then, we define a physics-informed conditional prior for the state path parameterization given the initial states and model parameters. After specifying a likelihood function to connect the unknown quantities to an experiment dataset, we update the posterior distribution of the state path parameterization and model parameters. Designing an expressive yet simple linear basis before knowing the true state path is crucial for inference accuracy but challenging. Moreover, reparameterizing the state path using the initial state is easy to perform for a linear basis, but is nontrivial for more complex and expressive function parameterizations, such as neural networks. The objective of this paper is to simplify and enrich the class of state path parameterizations using neural networks for the information field theory approach to Bayesian state and parameter estimation in dynamical systems. To this end, we propose a generalized physics-informed conditional prior using an auxiliary initial state. We show the existing reparameterization is a special case. We parameterize the state path using a residual neural network that consists of a linear basis function and a Fourier encoding fully connected neural network residual function. The residual function aims to correct the error of the linear basis function. To sample from the intractable posterior distribution, we develop an optimization algorithm, nested stochastic variational inference, and a sampling algorithm, nested preconditioned stochastic gradient Langevin dynamics. A series of numerical and experimental examples verify and validate the proposed method.

Keywords Information field theory · Physics-informed neural networks · Dynamical system · Bayesian state and parameter estimation · Uncertainty quantification

1 Introduction

Bayesian probabilistic state reconstruction and model parameter estimation for dynamical systems governed by ordinary differential equations are ubiquitous in mathematical and engineering problems. Such problems include nonlinear energy sink device [Lund et al., 2020], structural dynamics [Chatterjee et al., 2023, Nayek et al., 2023], structural damage identification [Li et al., 2023], polymer composite [Thomas et al., 2022], magnet synchronous machine [Beltran-Pulido et al., 2020], wind turbine [Song et al., 2018], building structure [Kosikova et al., 2023], building energy [Yi and Park, 2021], particle tracking velocimetry [Hao et al., 2023, 2024, Hans et al., 2024], and heating, ventilation, and air

*Corresponding author.

conditioning system [Hao, 2020, Hao et al., 2022]. The goal is to use noisy measurement data to estimate the unknown time evolution states and model parameters with uncertainty quantification and propagation into the future. Essential steps are specifying a prior distribution of the states and parameters, evaluating the likelihood given measurement data by running forward models, and computing the posterior distribution of the states and parameters.

Standard approaches, such as Kalman filters [Kalman, 1960, Wan and Van Der Merwe, 2000, Evensen, 2003, Anderson and Moore, 2012], particle filters [Liu and Chen, 1998, Doucet et al., 2000], and variational filters [Lund et al., 2021], can estimate the posterior distribution of dynamical model states from noisy measurements when model parameters are given. To jointly estimate the model states and parameters, we apply methods such as dual Kalman filter [Wan and Nelson, 1996, 2001] and nested particle filters [Chopin et al., 2013, Crisan and Miguez, 2018]. Despite the great success of these standard methods in the past, they do not exploit the revolutionary deep learning software, such as pytorch Paszke et al. [2019] and JAX [Bradbury et al., 2018], which leverage automatic differentiation [Paszke et al., 2017]. To apply the standard methods, we need to discretize the ordinary differential equations. Then, we have to repeatedly run ODE solvers to evaluate the predictive distribution and the likelihood function. Therefore, the standard approaches do not scale well with the dimensions of model states and parameters, and the size of measurement data.

Information field theory (IFT) [Enßlin et al., 2009, Enßlin, 2013, 2019, Alberts and Bilonis, 2023] is a Bayesian approach to reconstruct the infinite-dimensional physical fields, such as pressure and velocity fields. IFT applies the statistical field theory to encode the prior knowledge about the field, such as space-time homogeneity, temporal causality, and locality [Frank et al., 2021, Westerkamp et al., 2021]. Then, the likelihood function is constructed using a measurement response function that maps the physical fields to the measurement data. It is usually intractable to compute the posterior distribution of the physical fields, except for special cases such as Gaussian random field with linear measurement response function [Lancaster and Blundell, 2014]. Therefore, numerical approaches, such as the metric Gaussian variational inference [Knollmüller and Enßlin, 2019], are required to approximate the posterior distribution.

Hao and Bilonis [2024] introduced an information field theory approach to dynamical system state reconstruction and model parameter estimation, which leverages JAX software to accelerate numerical computation. To apply the method, the authors parameterize the time evolution state path using a finite number of linear bases. Next, they define a prior distribution for the state path parameterization and dynamical model parameters. This prior has a physics-informed conditional prior for the state path parameterization given the initial states and model parameters. IFT constructs this prior using the path integral technique Feynman et al. [2010], Zinn-Justin [2021], which is similar to energy-based models [Grenander and Miller, 1994]. Second, a likelihood function relates the state function and model parameters to a measurement dataset. Lastly, applying the Bayes’ rule, we can find the posterior distribution of the parameterized state path function and model parameters. The posterior is analytically intractable in general, so numerical methods are required. Alberts and Bilonis [2023] and Hao and Bilonis [2024] developed a sampling and an optimization approaches using stochastic gradient Langevin dynamics [Welling and Teh, 2011] and stochastic variational inference [Hoffman et al., 2013], respectively. The proposed method is computationally efficient and scalable for the following reasons. First, similar to physics-informed neural networks [Raissi et al., 2019], IFT randomly samples a collection of time points to evaluate the physics-informed conditional prior, which can be efficiently implemented using *vmap* and *jit* in JAX. The number of sampling time points is usually much less than the required discretized time grid to run ODE solvers recursively. Second, IFT subsamples a minibatch dataset from a large measurement dataset, so its scalability is superior. Despite the promising applications of IFT in the future, we notice that Hao and Bilonis [2024] reparameterizes the state path using the initial state. This reparameterization trick is easy to do for simple function parameterizations, such as the linear span of finite bases. However, for more complex and expressive parameterizations, such as neural networks, it is non-trivial. Hence, the requirement of reparameterization complicates and limits the choice of representing the state function.

The objective of this paper is to simplify and enrich the class of state path parameterizations using neural networks for the information field theory approach to Bayesian state and parameter estimation in dynamical systems. We call the method neural information field filter (NIFF). We introduce the generalized physics-informed conditional prior that does not need to reparameterize the state path using its initial states. We achieve this using an auxiliary initial state, which is not necessarily the same as the initial state of the state path function. We use a kernel Hamiltonian to measure the similarity between the auxiliary initial state and the initial state of the parameterized state path function. We show that the reparameterization trick using the initial state is a special case of the generalized physics-informed conditional prior when the kernel is the Dirac function. Specifically, we define the relaxed physics-informed conditional prior by choosing a Gaussian kernel. We parameterize the state path function using residual neural networks [He et al., 2016] that consist of a linear basis function and a residual function. The linear basis function is the same as specified in [Hao and Bilonis, 2024], and the residual function is a fully connected neural network with a Fourier encoding first-layer [Tancik et al., 2020, Hennigh et al., 2021]. The linear basis function inherits all the advantages of [Hao and Bilonis, 2024], such as mathematical form simplicity. However, designing a linear basis to achieve an

acceptable accuracy is not easy as we do not know all the properties, such as the regularity, of the unknown state path functions. The residual function complements the linear basis function by correcting the remaining errors and fine-tuning the estimated state path function. To numerically approximate the intractable posterior distribution of the state path parameterization and model parameters, we develop an optimization algorithm, nested stochastic variational inference, and a sampling algorithm, nested preconditioned stochastic gradient Langevin dynamics. Both methods apply Monte Carlo sampling techniques to update the unknown quantities computationally efficiently. Last, we verify and validate NIFF through a series of numerical and experimental examples.

The structure of this paper is as follows. In section 2, we review the information field theory approach to Bayesian state and parameter estimation in dynamical systems developed in [Hao and Bilonis, 2024]. In section 3, we theoretically develop NIFF. In section 4, we develop an optimization algorithm, nested stochastic variational inference, and a sampling algorithm, nested preconditioned stochastic gradient Langevin dynamics. In section 5, we verify and validate NIFF through a series of numerical and experimental examples. Last, section 6 concludes the paper.

2 Background on information field theory approach to Bayesian state and parameter estimation in dynamical systems

We review our previous work, the information field theory approach to dynamical system state reconstruction and parameter estimation [Hao and Bilonis, 2024]. In the following mathematical exposition, we change our original notation to emphasize the reparameterization step.

We consider the dynamical system governed by the ODE

$$\begin{aligned}\dot{x}(t) &= f(x(t), t; \theta), \\ Y(t_k) &= R(x(t_k); \theta) + \text{noise},\end{aligned}\tag{1}$$

where $x(t) \in \mathbb{R}^{d_x}$ is the state vector, f is the vector field, $\theta \in \mathbb{R}^{d_\theta}$ are the model parameters, R is the measurement response function and $Y(t_k) \in \mathbb{R}^{d_y}$ is the random output vector. The noise is usually independent, identically distributed, zero-mean Gaussian. The objective is to estimate the model parameters θ and time evolution state path $x(t)$ from a noisy measurement data $y = (y(t_1), \dots, y(t_{n_d}))$ at n_d sampling time points.

Hao and Bilonis [2024] parameterizes the state path function $x(t) = \hat{x}(t; w)$ using a $K + 1$ linear basis $\psi(t) = [\psi_0(t), \dots, \psi_K(t)]^T$ with the coefficient matrix $W = [w_0, \dots, w_K] \in \mathbb{R}^{d_x \times (K+1)}$. Notice that we vectorize this matrix into $w = \text{vec}(W)$ for notational simplicity. Then, the parameterized path is $\hat{x}(t; w) = \sum_i w_i \psi_i(t)$. We use this parameterized state path to define the physics-informed prior information Hamiltonian:

$$H(w, \theta) = \int_0^T dt \|\dot{\hat{x}}(t; w) - f(\hat{x}(t; w), t; \theta)\|^2.$$

Since IFT requires evaluating and sampling from the physics-informed conditional prior, which is conditioned on the initial state, we reparameterize $\hat{x}(t; w)$ explicitly using the initial state x_0 (refer to section 2.2 in [Hao and Bilonis, 2024]). This is achieved by solving the equation:

$$\sum_{i=0}^{K+1} w_i \psi_i(0) = x_0.$$

Choose one of the basis $\psi_i(t)$ as the dependent basis, its dependent coefficient vector is

$$w_i = \frac{x_0 - \sum_{j \neq i} w_j \psi_j(0)}{\psi_i(0)}.\tag{2}$$

We use the notation w_{-i} to denote the remaining free coefficients, i.e., $w_{-i} = \text{vec}([w_0, \dots, w_{i-1}, w_{i+1}, \dots, w_K])$, and concisely denote the function in Eq. (2) by $w_i = \mathcal{T}(x_0; w_{-i})$. We denote $w = (w_{-i}, w_i)$, so the reparameterized state path is

$$\begin{aligned}\tilde{x}(t; w_{-i}, x_0) &= \hat{x}(t; w_{-i}, \mathcal{T}(x_0; w_{-i})) \\ &= \mathcal{T}(x_0; w_{-i}) \psi_i(t) + \sum_{j \neq i} w_j \psi_j(t),\end{aligned}$$

and the reparameterized information Hamiltonian is

$$\begin{aligned}\tilde{H}(w_{-i}, x_0, \theta) &= \int_0^T \|\dot{\hat{x}}(t; w_{-i}, x_0) - f(\hat{x}(t; w_{-i}, x_0), t; \theta)\|^2 dt \\ &= \int_0^T \left\| \dot{\hat{x}}(t; w_{-i}, \mathcal{T}(x_0; w_{-i})) - f(\hat{x}(t; w_{-i}, \mathcal{T}(x_0; w_{-i})), t; \theta) \right\|^2 dt \\ &= H(w_{-i}, \mathcal{T}(x_0; w_{-i}), \theta).\end{aligned}$$

The objective of IFT is to find the posterior distribution:

$$p(w_{-i}, x_0, \theta | y) = \frac{p(y | w_{-i}, x_0, \theta) \tilde{p}(w_{-i} | x_0, \theta) p(x_0, \theta)}{p(y)},$$

where the physics-informed conditional prior is:

$$\tilde{p}(w_{-i} | x_0, \theta) = \frac{e^{-\beta \tilde{H}(w_{-i}, x_0, \theta)}}{Z(x_0, \theta)}. \quad (3)$$

In the above definition, β is a hyperparameter that controls our level of trust in the model. A greater β enforces the physics harder, and the normalization constant

$$Z(x_0, \theta) = \int e^{-\beta \tilde{H}(w_{-i}, x_0, \theta)} dw_{-i}$$

is the partition function. The essence of IFT is encoding well-known physics through the physics-informed conditional prior.

The reparameterization step is necessary since given the initial state x_0 and model parameter θ , the ODE defined in Eq. (1) has a unique solution under mild conditions [Meiss, 2007]. So, it is feasible to sample from the physics-informed condition prior $p(w | x_0, \theta)$. However, to reparameterize the state path function, we have to solve the system of equations in Eq. (2). This is trivial when $\hat{x}(t; w)$ is a finite linear basis but nontrivial for more expressive function parameterizations, such as neural networks. In the following, we extend IFT such that the reparameterization step is not required so we can use neural networks to enrich the state path parameterization.

3 Theoretical development

3.1 Generalized physics-informed conditional prior

We parameterize the state path using $\hat{x}(t; w)$ without reparameterization. First, we make the following definition.

Definition 1 (Generalized physics-informed conditional prior). Let x_0 be the auxiliary initial state variable, which is not necessarily equal to $\hat{x}(0; w)$. The generalized physics-informed conditional prior is

$$p(w | x_0, \theta) = \frac{e^{-\beta H(w, \theta) - H(\hat{x}(0; w), x_0)}}{Z(x_0, \theta)},$$

where the kernel Hamiltonian is

$$H(\hat{x}(0; w), x_0) = -\log K(\hat{x}(0; w), x_0),$$

and the normalization constant is

$$Z(x_0, \theta) = \int e^{-\beta H(w', \theta) - H(\hat{x}(0; w'), x_0)} dw'.$$

When the kernel Hamiltonian is not properly defined, e.g., when $K(\cdot, \cdot)$ is the Dirac function, we simply write $p(w | x_0, \theta) = K(\hat{x}(0; w), x_0) \frac{e^{-\beta H(w, \theta)}}{Z(x_0, \theta)}$.

To get the conditional prior $p(w | \theta)$, we marginalize out x_0 using a prior distribution for the auxiliary initial state:

$$p(w | \theta) = \int p(w | x_0, \theta) p(x_0) dx_0.$$

This step essentially performs the convolution against the kernel $K(\hat{x}(0; w), x_0)$.

The prior defined in Eq. (3) is a special case of the generalized physics-informed conditional prior when the Kernel $K(\hat{x}(0; w), x_0)$ is the Dirac function.

Proposition 1. Denote the marginal distribution of the generalized physics-informed conditional prior $p(w_{-i}|x_0, \theta) = \int p(w|x_0, \theta) dw_i$, and the joint distribution of the reparameterized prior $\tilde{p}(w|\theta) = \tilde{p}(w_{-i}|x_0, \theta)p(x_0)$. Define the function $w_i = \mathcal{T}(x_0; w_{-i})$ such that $\hat{x}(0; w_{-i}, \mathcal{T}(x_0; w_{-i})) = x_0$, and assume \mathcal{T} is bijective between x_0 and w_i . If the kernel is $K(\hat{x}(0; w), x_0) = \delta(w_i - \mathcal{T}(x_0; w_{-i}))$. Then $p(w_{-i}|x_0, \theta) = \tilde{p}(w_{-i}|x_0, \theta)$ and $p(w|\theta) = \tilde{p}(w|\theta)$. We recover the reparameterization approach in [Hao and Bilonis, 2024].

Proof is in Appendix A.

3.2 Relaxed physics-informed conditional prior

We choose the special Kernel

$$K(\hat{x}(0; w), x_0) = e^{-\beta_2 \|\hat{x}(0; w) - x_0\|^2},$$

and use $H(\hat{x}(0; w), x_0) = \|\hat{x}(0; w) - x_0\|^2$ to denote kernel Hamiltonian. Then, we define the relaxed physics-informed conditional prior:

$$p(w|x_0, \theta) = \frac{e^{-\beta_1 H(w, \theta) - \beta_2 H(\hat{x}(0; w), x_0)}}{Z(x_0, \theta)}. \quad (4)$$

The normalization constant is

$$Z(x_0, \theta) = \int e^{-\beta_1 H(w, \theta) - \beta_2 H(\hat{x}(0; w), x_0)} dw. \quad (5)$$

Remark 1. The relaxed physics-informed conditional prior has a probabilistic interpretation of the proximal operator [Parikh et al., 2014]. It takes higher probability when $H(w, \theta)$ is smaller and the state path initial point $\hat{x}(0; w)$ is closer to the auxiliary initial point x_0 .

Applying the Bayes' rule and integrating out the auxiliary initial state x_0 , the posterior distribution is

$$\begin{aligned} p(w, \theta|y) &= \int p(w, \theta, x_0|y) dx_0 \\ &= \int \frac{p(y|w, \theta)p(w|x_0, \theta)p(\theta)p(x_0)}{p(y)} dx_0. \end{aligned} \quad (6)$$

We plot two directed acyclic graphs in Fig. 1 to visualize the difference between our proposed method and the method in [Hao and Bilonis, 2024]. We use a circle to denote a node that is randomly generated from its parent nodes, and a square to denote a node that is deterministically generated from its parent nodes. In our relaxed method, the auxiliary initial state x_0 does not directly link to the measurement data y .

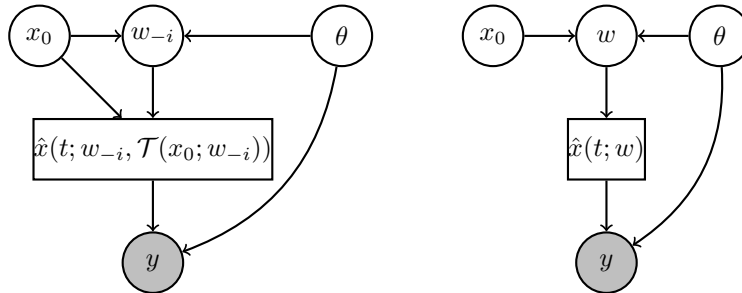


Figure 1: Directed acyclic graphs for the reparameterized state path approach [Hao and Bilonis, 2024] (left) and the relaxed physics-informed conditional prior approach (right).

3.2.1 Fourier encoding residual neural networks

We parameterize the state path $x(t) = \hat{x}(t; w)$ using neural networks. Due to the stochastic relaxation, we do not need to reparameterize it using the initial state x_0 . We use a hybrid parameterization that combines a linear basis $\sum_i w_i^b \psi_i(t)$ and a neural network, where the neural network aims to learn the residual state path. For the neural network part, we

pass the time variable through a Fourier feature encoding layer first [Tancik et al., 2020, Hennigh et al., 2021], since it helps to address the spectral bias issue in neural networks [Rahaman et al., 2019, Wang et al., 2022]. Specifically, we encode the time t to a $2K + 1$ high dimensional Fourier space with a \bar{T} time period using

$$\left(1, \sin \frac{2\pi t}{\bar{T}}, \cos \frac{2\pi t}{\bar{T}}, \dots, \sin \frac{2\pi Kt}{\bar{T}}, \cos \frac{2\pi Kt}{\bar{T}}\right) = T_{\text{encoder}}(t).$$

Let $T_i(z; w_i^{\text{NN}}) = \sigma_i(w_i^{\text{NN}}z + b_i)$ denote a neural network hidden layer, where w_i^{NN} is the weight matrix, b_i is the bias vector, and σ_i is the nonlinear activation. The hybrid parameterization consists of two parallel predictive paths using the linear basis and neural network functions. We collectively write $w = (w_{1:n_{\text{hidden}}}^{\text{NN}}, w_{\text{out}}^{\text{NN}}, w^b)$, and the hybrid parameterization is

$$\text{NN}(t; w) = T_{\text{out}} \circ T_{n_{\text{hidden}}} \circ T_{n_{\text{hidden}}-1} \circ \dots \circ T_1 \circ T_{\text{encoder}}(t; w_{1:n_{\text{hidden}}}^{\text{NN}}, w_{\text{out}}^{\text{NN}}) + \sum_i w_i^b \psi_i(t). \quad (7)$$

4 Numerical algorithms

In this section, we develop two numerical algorithms to sample from the posterior distribution $p(w, \theta|y)$ defined in Eq. (6). The first one is an optimization-based method called nested stochastic variational inference (NSVI). The second one is a Markov chain Monte Carlo sampling-based method called nested preconditioned stochastic gradient Langevin dynamics (NPSGLD). NSVI is computationally efficient, though less accurate, and can be applied to high-dimensional problems, such as those with more than ten thousand unknown variables. NPSGLD converges asymptotically theoretically, but the mixing time is unrealistically slow for high-dimensional problems. A practical guideline for selecting these two methods is that NSVI and NPSGLD are both suitable for low-dimensional problems, e.g., those with fewer than one thousand unknown variables. NPSGLD achieves better estimation results when NSVI uses a simple approximation probability distribution, such as a diagonal multivariate Gaussian. For high-dimensional problems, we recommend the NSVI method as it converges fast, albeit with approximation errors.

The relaxed physics-informed conditional prior defined in Eq. (4) contains the initial state and model parameter-dependent normalization constant $Z(x_0, \theta)$. Since both NSVI and NPSGLD have to take the gradient of $\log Z(x_0, \theta)$, we define the unnormalized relaxed physics-informed conditional prior

$$\pi(w|x_0, \theta) = e^{-\beta_1 H_1(w, \theta) - \beta_2 H_2(\hat{x}(0; w), x_0)}$$

to write

$$p(w|x_0, \theta) = \frac{\pi(w|x_0, \theta)}{Z(x_0, \theta)}.$$

4.1 Nested stochastic variational inference

4.1.1 Background on variational inference

In variational inference, we want to find an optimal parameterized guide $q_\phi(z)$, e.g., a normal distribution, to approximate a posterior distribution $p(z|y) = \frac{p(y, z)}{p(y)}$. Variational inference achieves this by minimizing the Kullback-Leibler (KL) divergence [Kullback and Leibler, 1951] between the guide and the posterior distribution:

$$\min_{\phi} D_{\text{KL}}(q_\phi(z)||p(z|y)) = \mathbb{E}_{q_\phi(z)} \left[\log \frac{q_\phi(z)}{p(z|y)} \right].$$

The KL divergence $D_{\text{KL}}(q_\phi(z)||p(z|y))$ is nonnegative. When it equals to zero, $q_\phi(z) = p(z|y)$ almost everywhere.

However, evaluating the KL divergence is computationally impossible as the evidence $p(y)$ is intractable. An alternative approach is to maximize a dual objective function called evidence lower bound (ELBO) [Jordan et al., 1999, Kingma and Welling, 2013]:

$$\max_{\phi} \text{ELBO}(\phi|y) = \mathbb{E}_{q_\phi(x)} \left[\log \frac{p(y, z)}{q_\phi(z)} \right].$$

Maximizing the ELBO is equivalent to minimizing $D_{\text{KL}}(q_\phi(z)||p(z|y))$, and we only need to evaluate $p(y, z)$ instead of $p(z|y)$.

4.1.2 Nested stochastic variational inference to approximate the marginal posterior $p(w, \theta|y)$

We parameterize the guide $q_\phi(w)$ and $q_\psi(\theta)$ to approximate $p(w, \theta|y)$. Additionally, we specify a guide $q_\chi(x_0)$ to the auxiliary initial state. Typically, measurement data y satisfies the conditionally independent assumption, i.e.,

$$\log p(y|w, \theta) = \sum_{i=1}^{n_d} \log p(y_i|\hat{x}(t_i; w), \theta).$$

To scale to a large dataset, we subsample a minibatch of indices \mathcal{I}_{m_d} of size m_d from the set $\{1, \dots, n_d\}$ with a probability of $\binom{n_d}{m_d}^{-1}$.

The objective of NSVI is to maximize the ELBO:

$$\begin{aligned} \max_{\phi, \psi, \chi} \text{ELBO}(\phi, \psi, \chi|y) = & + \mathbb{E}_{q_\phi(w)q_\psi(\theta)q_\chi(x_0)p(\mathcal{I}_{m_d})} \left[\frac{n_d}{m_d} \sum_{i \in \mathcal{I}_{m_d}} \log p(y_i|w, \theta) + \log \left\{ \frac{\pi(w|x_0, \theta)p(x_0, \theta)}{q_\phi(w)q_\psi(\theta)q_\chi(x_0)} \right\} \right] \\ & - \mathbb{E}_{q_\phi(w)q_\psi(\theta)q_\chi(x_0)} [\log Z(x_0, \theta)] \end{aligned} \quad (8)$$

A justification of this objective is in Appendix B.

Maximizing this ELBO requires taking the gradient of the log partition function. This is not trivial, as the partition function is defined using a high-dimensional integration Eq. (5). We devise an inner loop auxiliary stochastic variational inference, i.e., a nested loop, to sample from the relaxed physics-informed conditional prior. We leave the tedious numerical implementation details in Appendix C.

4.2 Nested preconditioned stochastic gradient Langevin dynamics

4.2.1 Background on preconditioned stochastic gradient Langevin dynamics

MCMC sampling from a posterior distribution $p(z|y)$ using unadjusted overdamped Langevin dynamics [Langevin, 1908] applies the following update step:

$$\Delta z_k = \rho_k (\nabla_z \log p(y|z_k) + \nabla_z \log p(z_k)) + \sqrt{2\rho_k} \xi_k,$$

where ρ_k is the learning rate, and ξ_k follows a multivariate diagonal Gaussian $\mathcal{N}(0, I)$. The step size ρ_k should satisfy the Robbins-Monro conditions [Robbins and Monro, 1951]

$$\sum_k \rho_k = \infty, \quad \sum_k \rho_k^2 < \infty$$

to converge to a local maximum.

To scale to a large data set, the stochastic gradient Langevin dynamics (SGLD) subsamples the measurement data, and the update step is [Welling and Teh, 2011]

$$\Delta z_k = \rho_k \left(\frac{n_d}{m_d} \sum_{i=1}^{m_d} \nabla_z \log p(y_i|z_k) + \nabla_z \log p(z_k) \right) + \sqrt{2\rho_k} \xi_k.$$

One of the issues in stochastic gradient Langevin dynamics is that the step sizes for all variables are the same. This may cause the updated step sizes for different variables in several orders of magnitude differences. Hence, instability and uneven convergence rate issues exist. A solution is preconditioned stochastic gradient Langevin dynamics (PSGLD), which pre-multiplies an adaptively-updated preconditioning matrix $M(z_k)$ to the Langevin dynamics. One approach is stochastic gradient Riemannian Langevin dynamics, whose update rule is [Patterson and Teh, 2013]

$$\Delta z_k = \rho_k \left(M(z_k) \left(\frac{n_d}{m_d} \sum_{i=1}^{m_d} \nabla_z \log p(y_i|z_k) + \nabla_z \log p(z_k) \right) + \Gamma(z_k) \right) + M(z_k)^{\frac{1}{2}} \sqrt{2\rho_k} \xi_k,$$

where $\Gamma_i(z_k) = \sum_j \partial_j \log p(y_j|z_k)$. When $M(z_k)$ is full rank, computing $\Gamma(z_k)$ is numerically expensive. We use a cheaper but still effective method, diagonal precondition strategy [Li et al., 2016], which uses the RMSprop rule [Hinton et al., 2012]:

$$\begin{aligned} V(z_k) &= \alpha V(z_{k-1}) + (1 - \alpha)g(z_k) \odot g(z_k), \\ M(z_k) &= \text{diag} \left(\frac{1}{\delta + \sqrt{V(z_k)}} \right). \end{aligned}$$

In the above equation, we define

$$g(z_k) = \frac{1}{m_y} \sum_{i \in I_{m_d}} \nabla_z \log p(y_i | z_k),$$

where \odot denotes the element-wise matrix product. This precondition strategy helps to keep the updated step sizes for different parameters in the same order of magnitude. The two hyper-parameters are α which decides the memorizing size, and δ which helps to avoid the numerical instability issue when $V(z_k)$ closes to zero and controls the extremes of the curvature in the preconditioner [Li et al., 2016].

4.2.2 NPSGLD to sample from the marginal posterior $p(w, \theta | y)$

To sample from the marginal posterior $p(w, \theta | y)$, we first sample $\{w_k, \theta_k, x_{0,k}\}$ from the joint posterior $p(w, \theta, x_0 | y)$, and only keep $\{w_k, \theta_k\}$ to marginalize out x_0 . We use the shorthand notation $M_k = M(w_k, x_{0,k}, \theta_k)$ and $\Gamma_k = \Gamma(w_k, x_{0,k}, \theta_k)$, then the update step is

$$\begin{aligned} [\Delta w_k, \Delta \theta_k, \Delta x_{0,k}] = & + \rho_k \left(M_k \left(\frac{n_d}{m_d} \sum_{i=1}^{m_d} \nabla_{w, \theta} \log p(y_i | w_k, \theta_k) + \nabla_{w, \theta, x_0} \log \frac{\pi(w_k | x_{0,k}, \theta_k) p(x_{0,k}, \theta_k)}{Z(x_{0,k}, \theta_k)} \right) + \Gamma_k \right) \\ & + M_k^{\frac{1}{2}} \sqrt{2\rho_k} \xi_k. \end{aligned} \quad (9)$$

Similar to NSVI, the update rule requires taking the gradient of the log partition function. We devise an inner loop auxiliary preconditioned stochastic gradient Langevin dynamics, i.e., a nested loop. The precondition matrix M_k also depends on the log partition function. We leave the numerical implementation details in Appendix D.

5 Numerical examples

In this section, we conduct several synthetic examples to verify and validate NIFF. In section 5.1, we consider a synthetic example based on a single-degree-of-freedom Duffing oscillator. This example is the same as one example from [Hao and Bilonis, 2024]. We use this example to compare and verify the proposed non-reparameterized state path function approach in this paper with the reparameterized state path function approach published in [Hao and Bilonis, 2024]. In section 5.2, we study the improvement using a residual path to parameterize the state path function. Specifically, we use a two-degree-of-freedom nonlinear system considered in [Kong et al., 2022]. In section 5.3, we demonstrate the performance of NIFF on a high-dimensional twenty-story frame structure model problem. In section 5.4, we validate NIFF using an experimental nonlinear energy sink problem. In all examples, we report 90% quantile posterior and predictive results. The computational costs for experimental examples are in Appendix F.

5.1 Comparison between reparameterized and non-reparameterized state path functions

In this example, we verify the proposed relaxed physics-informed conditional prior approach by comparing it to the reparameterized approach developed in [Hao and Bilonis, 2024]. We use the same Duffing oscillator example in section 3.3 of [Hao and Bilonis, 2024].

The Duffing oscillator is described by the equations:

$$\begin{aligned} \dot{x}_1(t) &= x_2(t), \\ \dot{x}_2(t) &= -k_1 x_2(t) - k_2 x_1(t) - k_3 x_1(t)^3 + \gamma \cos(\omega t), \\ Y(t) &= x_1(t) + \sigma_y V(t). \end{aligned}$$

It describes a damped oscillator undergoing a nonlinear restoring force term $k_3 x_1(t)^3$. The oscillator is excited by a cosine signal with a known amplitude γ of 0.37 m and a frequency ω of 1.2 rad/s. To reconstruct the state function and model parameters, we use the position measurement, which is perturbed by a scaled white noise process $\sigma_y V(t)$.

The reference true parameter values are $k_1 = 0.3$, $k_2 = -1$, and $k_3 = 1$. To improve the numerical stability, we normalize the state variables, model parameters and measurement data by the constants $(\bar{x}_1, \bar{x}_2) = (1.5, 1)$, $(\bar{k}_1, \bar{k}_2, \bar{k}_3) = (1, 1, 1)$, and $\bar{y} = 1.5$.

To prepare the synthetic measurement data, we ran a 50-second forward simulation using the Runge-Kutta method [Press, 2007] with a time step of 0.01s. The initial states are $(x_1(0), x_2(0))^T = (1, 0)^T$. The measurement noise standard deviations are set to 5% of the measurement normalization constant.

We parameterize the state function using the truncated Fourier series

$$\hat{x}(t; w) = w_0 + \sum_{k=1}^K \left(w_{2k-1} \sin \frac{2\pi k}{T} t + w_{2k} \cos \frac{2\pi k}{T} t \right) \quad (10)$$

with $K = 40$. We do not include a residual path as this example aims to verify the proposed non-reparameterized state path function method.

We compare the posterior distributions solved by four methods. For all four cases, the prior distributions for the model parameters, initial states and the auxiliary initial states are standard Normal distributions. The individual setups are as follows.

First, we use the reparameterized state function approach in [Hao and Bilonis, 2024] and solve it using NSVI. We choose a diagonal Normal distribution as the guide for the Fourier coefficients and the initial state. The guide for the model parameters is a full-rank Normal distribution. The inverse temperature $\beta = 200$. The optimization step-ups, such as the learning rate and sample sizes, are chosen the same as in [Hao and Bilonis, 2024].

Second, we use the method proposed in this paper, i.e., the relaxed physics-informed conditional prior, and solve it using NSVI. We choose a diagonal Normal distribution as the guide for the Fourier coefficients and the auxiliary initial state. The guide for the model parameters is a full-rank Normal distribution. We set the hyperparameters $\beta_1 = 200$ and $\beta_2 = 100,000$. The sample sizes defined in Algorithm 4 are $(n_{\epsilon\eta\zeta}, n_t, \tilde{n}_\epsilon, \tilde{n}_t, m_y) = (1, 10, 1, 10, 10)$. The initial learning rate is 0.001 and we exponentially decay it every 100,000 iterations with a ratio of 0.1. We use the Adam algorithm [Kingma and Ba, 2014] to update the guide parameters. The Adam parameters are set to default, i.e., $b_1 = 0.9$, $b_2 = 0.999$.

Third, we use the relaxed physics-informed conditional prior and solve it using NSGLD developed in [Alberts and Bilonis, 2023]. We initialize three MC chains and sample them in parallel for 2×10^6 steps. We use the same hyperparameters $\beta_1 = 200$ and $\beta_2 = 100,000$. The sample sizes are the same as in case two. The learning rates for all parameters are 10^{-6} and kept constant throughout the sampling.

Last, we use the relaxed physics-informed conditional prior and solve it using NPSGLD. The sample sizes are the same as in case two. Due to the preconditioning matrix, we can use more aggressive step sizes at the early sampling stage. We set the initial step size to 10^{-4} and incorporate an exponential decay scheduler that decays the learning rate to 10^{-5} after 10^6 iterations and fix it for the remaining iterations. The hyper-parameter of the preconditioning matrix $\delta = 0.1$, and the initial memorizing size $\alpha = 0.99$ which is annealed to 1 after 10^6 iterations.

Figs 2 and 3 plot the posterior distributions of the state function and model parameters for the four methods. For the three sampling approaches, we only keep the final 10^6 samples and thin the samples every 1000 steps. The uncertainty of the state function x_2 is much higher than the uncertainty of x_1 , since we only measure x_1 . The results show a great agreement of the four methods. Fig 4 plots the convergence speeds of the parameter posterior distributions. The upper half shows the results for the entire 2×10^6 iterations. The lower half shows the zoomed-in results for the first 10^5 iterations. The plots show that NSVI converges faster than NSGLD and NPSGLD. Remarkably, NPSGLD significantly improves the convergence speed compared to NSGLD. Fig 5 compares the posterior distribution of the initial state of the parameterized state path function $p(\hat{x}(0; w)|y)$ to the posterior distribution of the auxiliary initial state $p(x_0|y)$. Since NSVI is an approximation approach, the two distributions slightly differ from each other. The NSGLD and NPSGLD show negligible differences between the two distributions.

5.2 Improvement using a residual path

In this example, we investigate the improvement in state reconstruction and parameter estimation accuracy by including a residual path in neural networks. We use a two-degree-of-freedom nonlinear system considered in [Kong et al., 2022]. The system consists of two masses. The mass m_1 is connected to the wall through a linear damper and a linear-plus-cubic (Duffing) nonlinear spring. The mass m_2 is connected to the mass m_1 through a linear spring and a linear-plus-cubic nonlinear damper. We excite the mass m_1 by a sinusoidal signal. The absolute displacements of m_1 and m_2 are denoted by y_1 and y_2 . We define the new displacement variables $q_1 = y_1$ and $q_2 = y_2 - y_1$ to write the governing equations:

$$\begin{bmatrix} m_1 & 0 \\ m_2 & m_2 \end{bmatrix} \begin{bmatrix} \ddot{q}_1 \\ \ddot{q}_2 \end{bmatrix} + \begin{bmatrix} c_1 & -c_2 \\ 0 & c_2 \end{bmatrix} \begin{bmatrix} \dot{q}_1 \\ \dot{q}_2 \end{bmatrix} + \begin{bmatrix} k_1 & -k_2 \\ 0 & k_2 \end{bmatrix} \begin{bmatrix} q_1 \\ q_2 \end{bmatrix} + \begin{bmatrix} k_1 \epsilon_1 q_1^3 - c_2 \epsilon_2 \dot{q}_2^3 \\ c_2 \epsilon_2 \dot{q}_2^3 \end{bmatrix} = \begin{bmatrix} F_0 \sin(\omega_0 t) \\ 0 \end{bmatrix}.$$

Let $x_1 = q_1$, $x_2 = \dot{q}_1$, $x_3 = q_2$ and $x_4 = \dot{q}_2$, we can easily write down a state space model with four state variables. We measure the displacements q_1 and $q_1 + q_2$ of m_1 and m_2 , respectively.

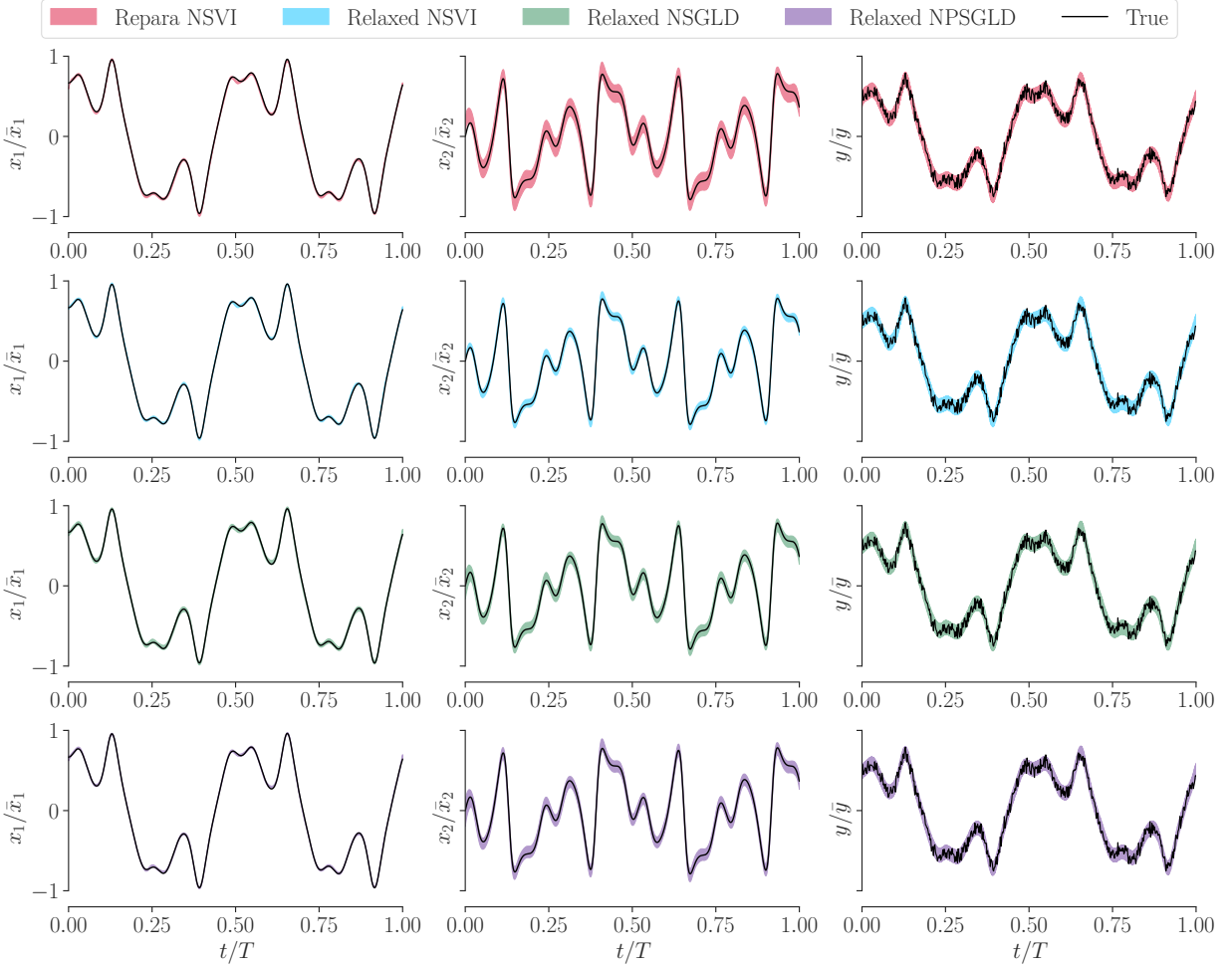


Figure 2: Example of section 5.1: posterior distributions of the states and measurement.

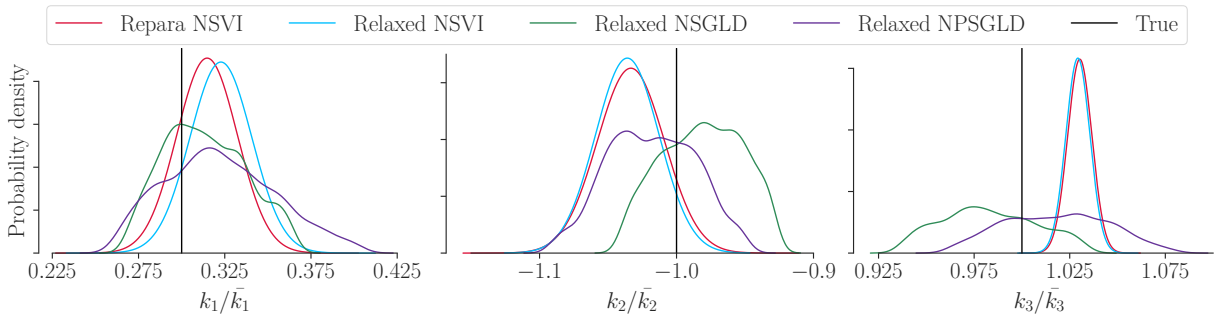


Figure 3: Example of section 5.1: posterior distributions of the model parameters.

The reference true parameter values are $m_1 = m_2 = 1$, $c_1 = c_2 = 0.2$, $k_1 = k_2 = 1$, and $\epsilon_1 = \epsilon_2 = 0.2$. We normalize all the eight parameters and the four states by 1. The normalization constants for the measurements are $(\bar{y}_1, \bar{y}_2) = (1, 2)$.

To prepare the synthetic measurement data, we ran a 50-second forward simulation using the Runge-Kutta method with a time step of 0.1s. The initial states are $(x_1(0), x_2(0), x_3(0), x_4(0))^T = (0, 0, 0.5, 0)^T$. The measurement noise standard deviations are set to 5% of the measurement normalization constant.

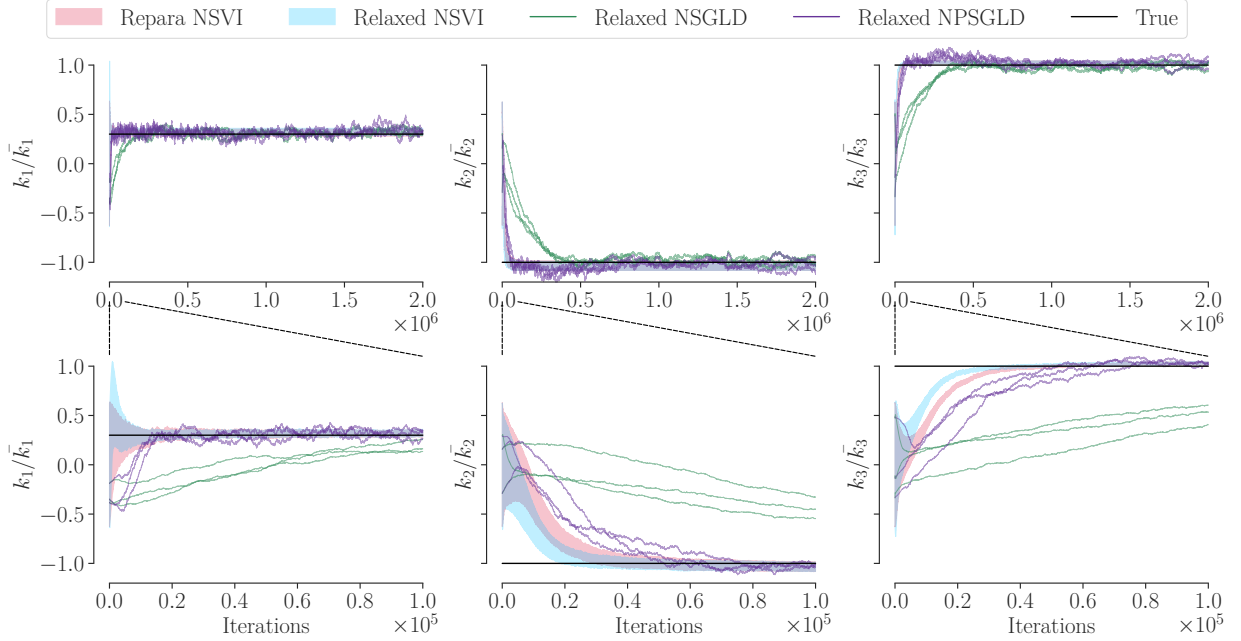


Figure 4: Example of section 5.1: convergence speeds of the model parameter posterior.

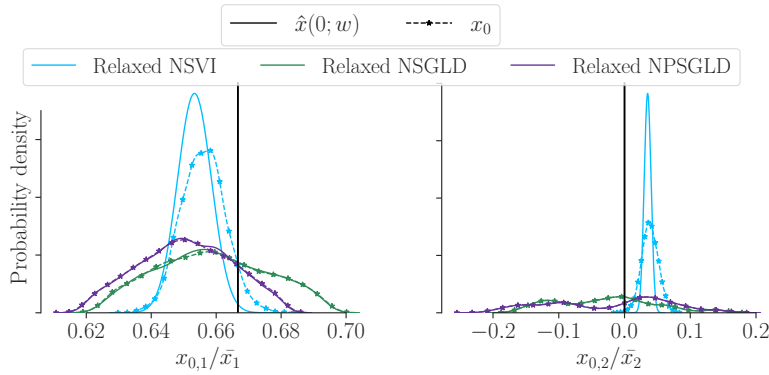


Figure 5: Example of section 5.1: posterior distributions of the state path initial state $\hat{x}(0; w)$ and the auxiliary initial state x_0 .

In terms of the parameterized state path function, the identity path is a radial basis

$$\hat{x}(t; w) = \sum_{k=1}^{K_b} w_k e^{-\frac{(x-z_k)^2}{2\sigma_k^2}},$$

where z_k and σ_k are location and scale parameters. Specifically, we choose $K_b = 20$ and $\sigma_k = 0.05$. The location parameters z_k are evenly spaced from 0 to 1. The residual path has a Fourier encoding layer with $K = 10$, one hidden layer of a width of 10, and the swish activation function [Ramachandran et al., 2017]. We designed this parameterization since the capacity of the radial basis is not enough to approximate the ground truth state path, and we hope the residual path can correct this unknown error.

We ran four cases, including with or without the residual path solved by NSVI or NPSGLD. In terms of the optimization setting, for NSVI, we ran 300,000 iterations and annealed the partition function in the ELBO during the first 200,000 iterations. The other optimization setups are the same as the previous example. For the NPSGLD, we ran 3 MC chains in parallel for 3,000,000 steps, burned the first 1,000,000 samples, and thinned the MC chain every 10,000 samples. The other optimization setups are the same as before.

Fig. 6 plots the comparison of the posterior and predictive distributions of the four states and two measurements using NSVI and NPSGLD. The left column is the result of NSVI, and the right column is the result of NPSGLD. We further split each subplot into the left part, showing the posterior distribution, and the right part, showing the posterior predictive distribution. We plot with or without the residual path in the same subplot. It is clear that the radial basis can not correctly reconstruct the state path while, by including the residual path, both NSVI and NPSGLD successfully reconstruct the state path. Fig. 7 plots the comparison of the posterior distribution of the eight model parameters using NSVI and NPSGLD. Similarly, with the residual path, the posterior distributions of the two algorithms, shown in green and purple, are close to the ground truth values. However, without the residual path, both algorithms fail to identify correct parameter values. We used the parameter posterior distribution to get a posterior predictive distribution of the four states and two measurements shown in Fig. 6. We observe the improvement of using a residual path. Finally, Fig. 8 plots the convergence speeds of the parameters. We observe the convergence speed of NPSGLD is fairly acceptable compared to NSVI. Moreover, the results of NSVI and NPSGLD with the residual path, shown in green and purple, show great agreement.

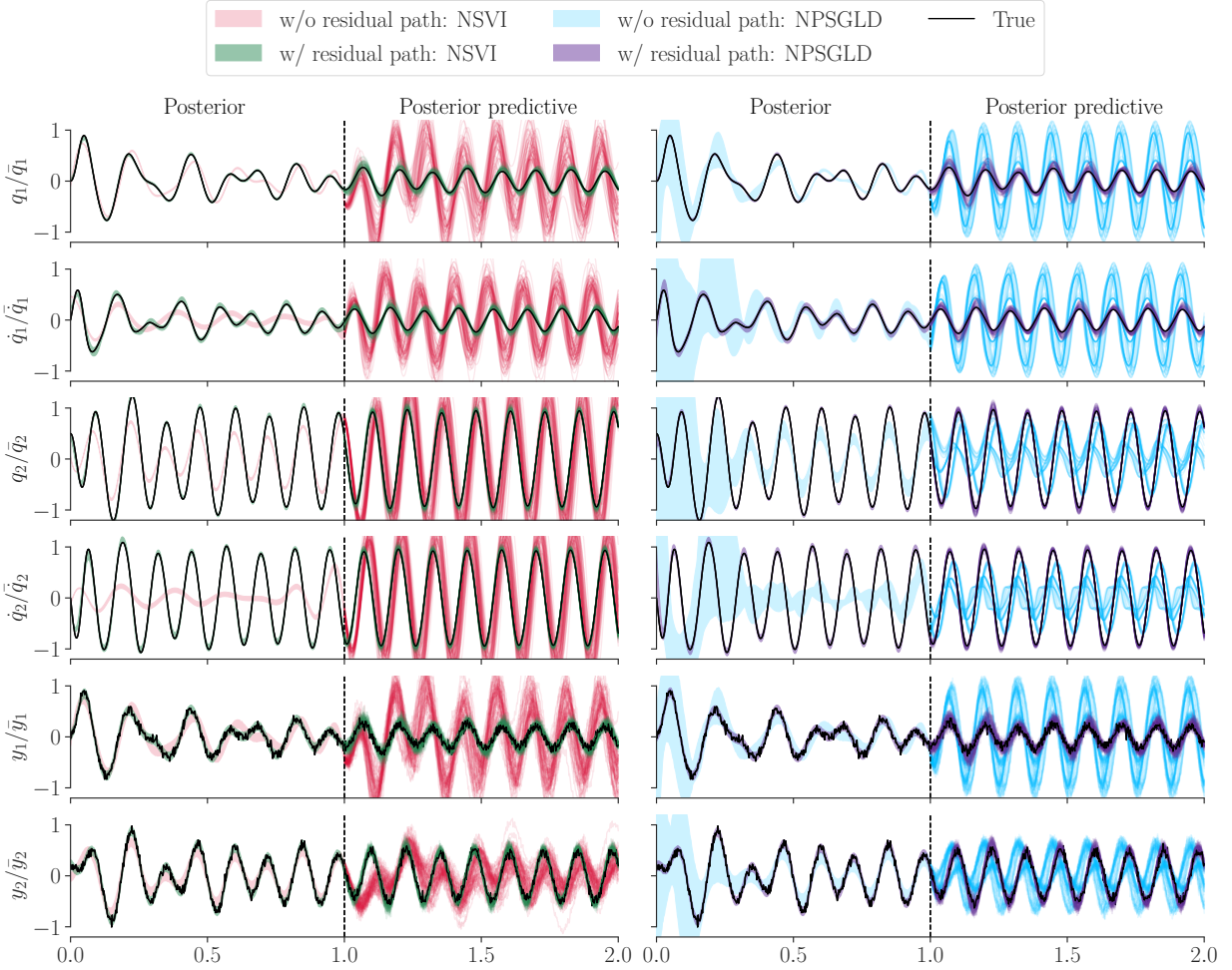


Figure 6: Example of section 5.2: posterior and predictive distributions of the states and measurements.

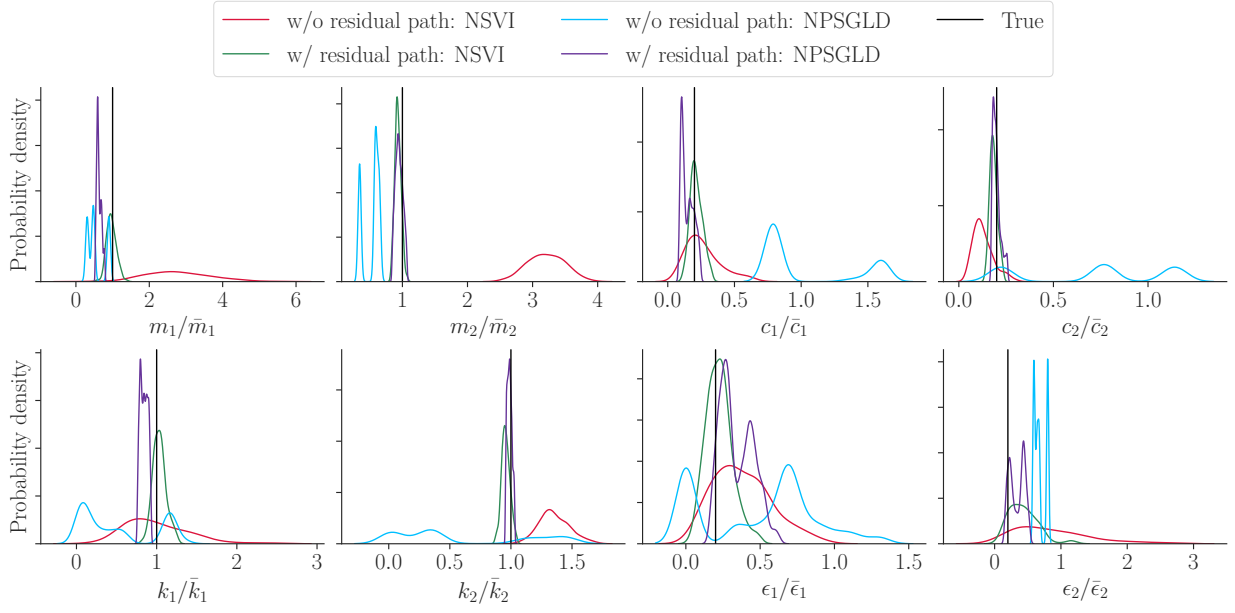


Figure 7: Example of section 5.2: posterior distributions of the parameters.

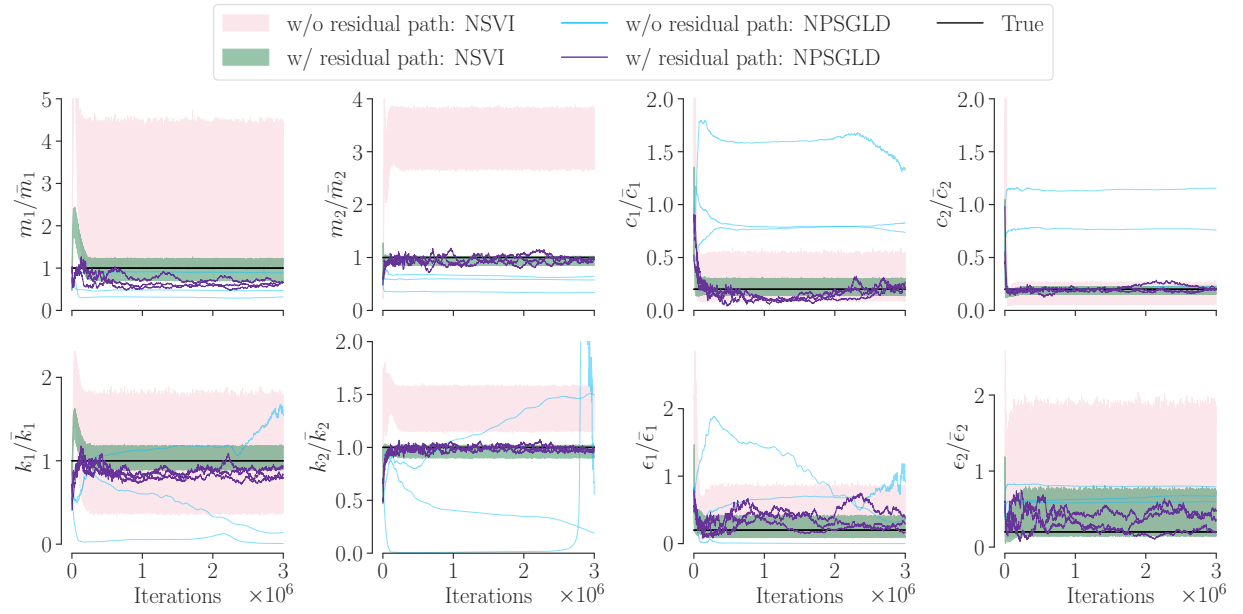


Figure 8: Example of section 5.2: convergence speeds of the model parameter posterior.

5.3 High-dimensional problem: a twenty-story frame structure

In this example, we study a twenty-story Bouc-Wen frame structure as a high-dimensional problem modified from [Li et al., 2024]. The dynamic equation is

$$\begin{aligned} \begin{bmatrix} m_1 & & & \\ & m_2 & & \\ & & \ddots & \\ & & & m_{20} \end{bmatrix} \begin{bmatrix} a_1 \\ a_2 \\ \vdots \\ a_{20} \end{bmatrix} + \begin{bmatrix} c_1 + c_2 & -c_2 & & \\ -c_2 & c_2 + c_3 & -c_3 & \\ & & \ddots & -c_{20} \\ & & & -c_{20} & c_{20} \end{bmatrix} \begin{bmatrix} v_1 \\ v_2 \\ \vdots \\ v_{20} \end{bmatrix} \\ + \begin{bmatrix} s_1 + s_2 & -s_2 & & \\ -s_2 & s_2 + s_3 & -s_3 & \\ & & \ddots & -s_{20} \\ & & & -s_{20} & s_{20} \end{bmatrix} \begin{bmatrix} z_1 \\ z_2 \\ \vdots \\ z_{20} \end{bmatrix} = - \begin{bmatrix} m_1 \\ m_2 \\ \vdots \\ m_{20} \end{bmatrix} a_g, \end{aligned}$$

where $a_{1:20}$ and $v_{1:20}$ are acceleration and velocity for each story, respectively. The system input a_g is the ground acceleration. The hysteretic displacement z is, for $l = 2, \dots, 20$,

$$\dot{z}_l = (v_l - v_{l-1}) - \beta |v_l - v_{l-1}| |z_l|^{n-1} z_l - \gamma (v_l - v_{l-1}) |z_l|^n,$$

and for $l = 1$

$$\dot{z}_1 = v_1 - \beta |v_1| |z_1|^{n-1} z_1 - \gamma v_1 |z_1|^n.$$

The Bouc-Wen parameters are β , γ and n .

The acceleration of each story is the measurement:

$$\begin{bmatrix} a_1 \\ \vdots \\ a_{20} \end{bmatrix} = - \begin{bmatrix} a_g \\ \vdots \\ a_g \end{bmatrix} - \begin{bmatrix} \frac{1}{m_1} & & & \\ & \ddots & & \\ & & \ddots & \\ & & & \frac{1}{m_{20}} \end{bmatrix} \left(\begin{aligned} & + \begin{bmatrix} c_1 + c_2 & -c_2 & & \\ -c_2 & c_2 + c_3 & -c_3 & \\ & & \ddots & -c_{20} \\ & & & -c_{20} & c_{20} \end{bmatrix} \begin{bmatrix} v_1 \\ v_2 \\ \vdots \\ v_{20} \end{bmatrix} \\ & + \begin{bmatrix} s_1 + s_2 & -s_2 & & \\ -s_2 & s_2 + s_3 & -s_3 & \\ & & \ddots & -s_{20} \\ & & & -s_{20} & s_{20} \end{bmatrix} \begin{bmatrix} z_1 \\ z_2 \\ \vdots \\ z_{20} \end{bmatrix} \end{aligned} \right).$$

We set $m_{1:20} = 1$ kg, $c_{1:20} = 0.25$ Ns/m, and randomly sampled the twenty stiffnesses $s_{1:20}$ from a uniform distribution $\mathcal{U}([8, 10])$. We assume $m_{1:20}$ and $c_{1:20}$ are given and only estimate $s_{1:20}$. To generate a synthetic measurement dataset, we used the first 5-second El-Centro NS earthquake signal <https://www.vibrationdata.com/elcentro.htm> as the ground acceleration a_g . We corrupted the measurement data $a_{1:20}$ by zero-mean Gaussian noises whose standard deviations are 1% of the root-mean-square values of the story accelerations.

The state path is parameterized by a 100 evenly spaced radial basis with a 0.01 length scale. The residual path has a Fourier encoding layer with $K = 10$, one hidden layer of a width of 10, and the swish activation function.

We ran NSVI 50,000 steps and NPSGLD 200,000 steps with 5 chains, respectively. The setups of the two algorithms are similar to the previous section. Figs. 9-12 plot the posterior distributions of velocities, hysteretic displacements, accelerations and stiffnesses. We observe that both algorithms successfully reconstruct the 40 states. In terms of the stiffness parameters, NPSGLD identifies all $s_{1:20}$ with negligible errors. NSVI identifies s_1 and $s_{3:20}$ with negligible errors, albeit s_2 has a small error. We use the entire 30-second ground acceleration data to check the posterior predictive distribution. Fig. 13 plots the result for story frames 1, 5, 10, 15, and 20. The prediction result is accurate despite z_{15} and z_{20} showing small errors.

5.4 Experimental example: nonlinear energy sink device

Last, we validate NIFF using a nonlinear energy sink device experimental example. The experimental detail and data have been published in [Silva et al., 2019]. The nonlinear energy sink device is a Duffing-type oscillator, which is designed to transfer and dissipate energy. Lund et al. [2021] used unscented Kalman filter [Wan and Van Der Merwe, 2000] to identify a mathematical model for the nonlinear energy sink device from experimental data. The model is

$$m\ddot{x} + c_\nu \dot{x} + c_f \tanh(200\dot{x}) + kx + zx^3 = -m\ddot{x}_g, \quad (11)$$

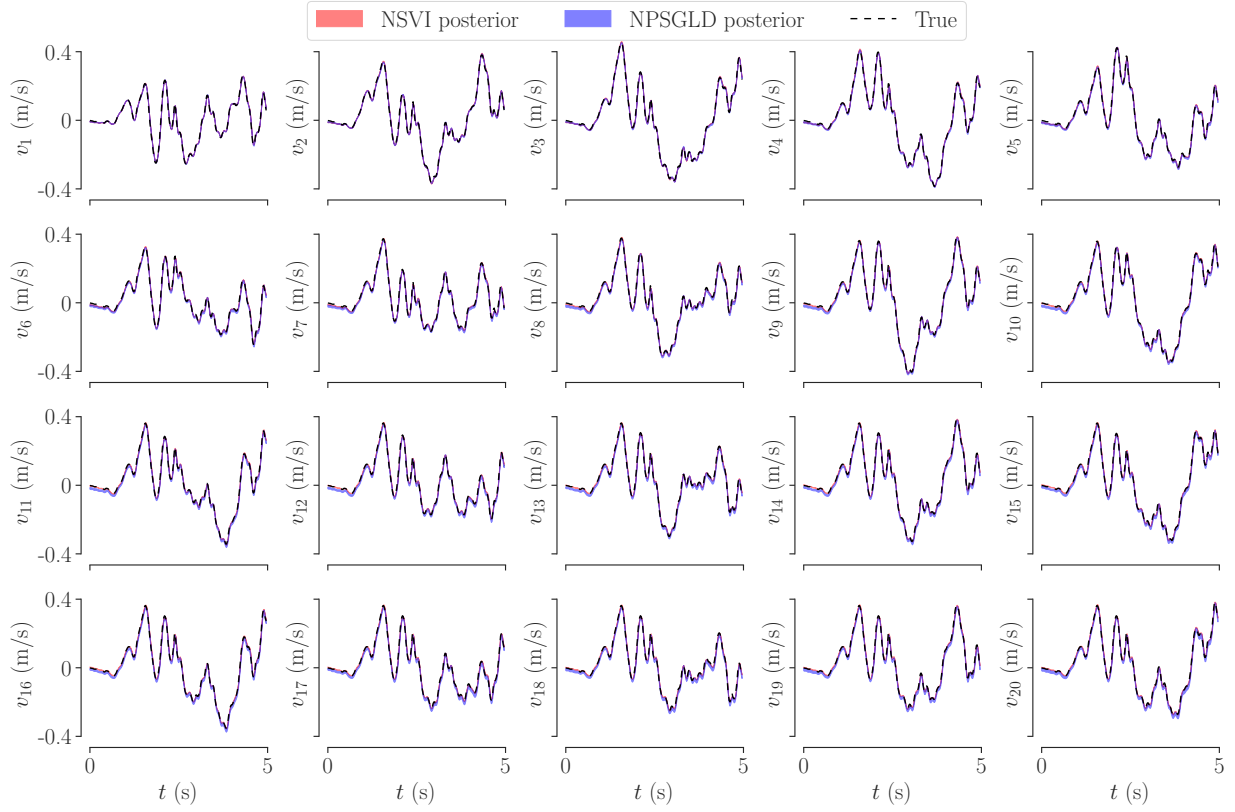


Figure 9: Example of section 5.3: NSVI and NPSGLD posterior distributions of velocities.

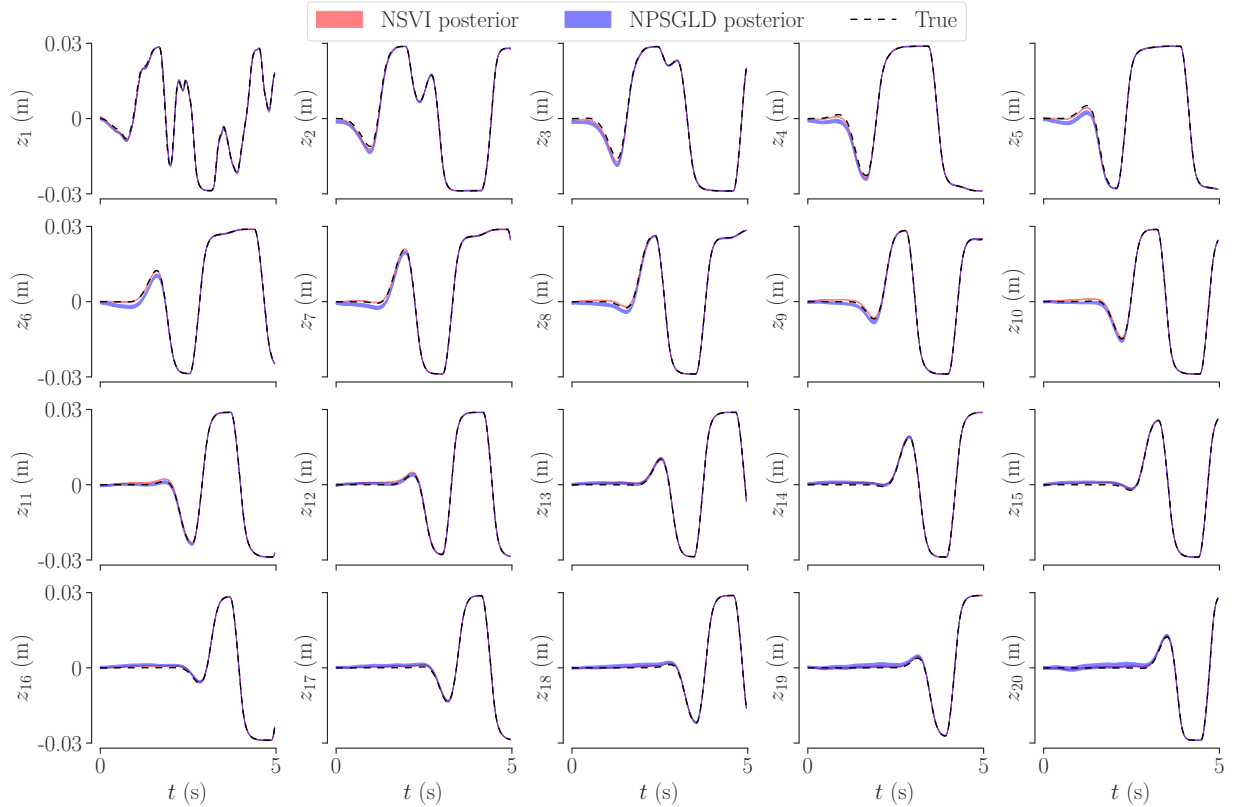


Figure 10: Example of section 5.3: NSVI and NPSGLD posterior distributions of hysteretic displacements.

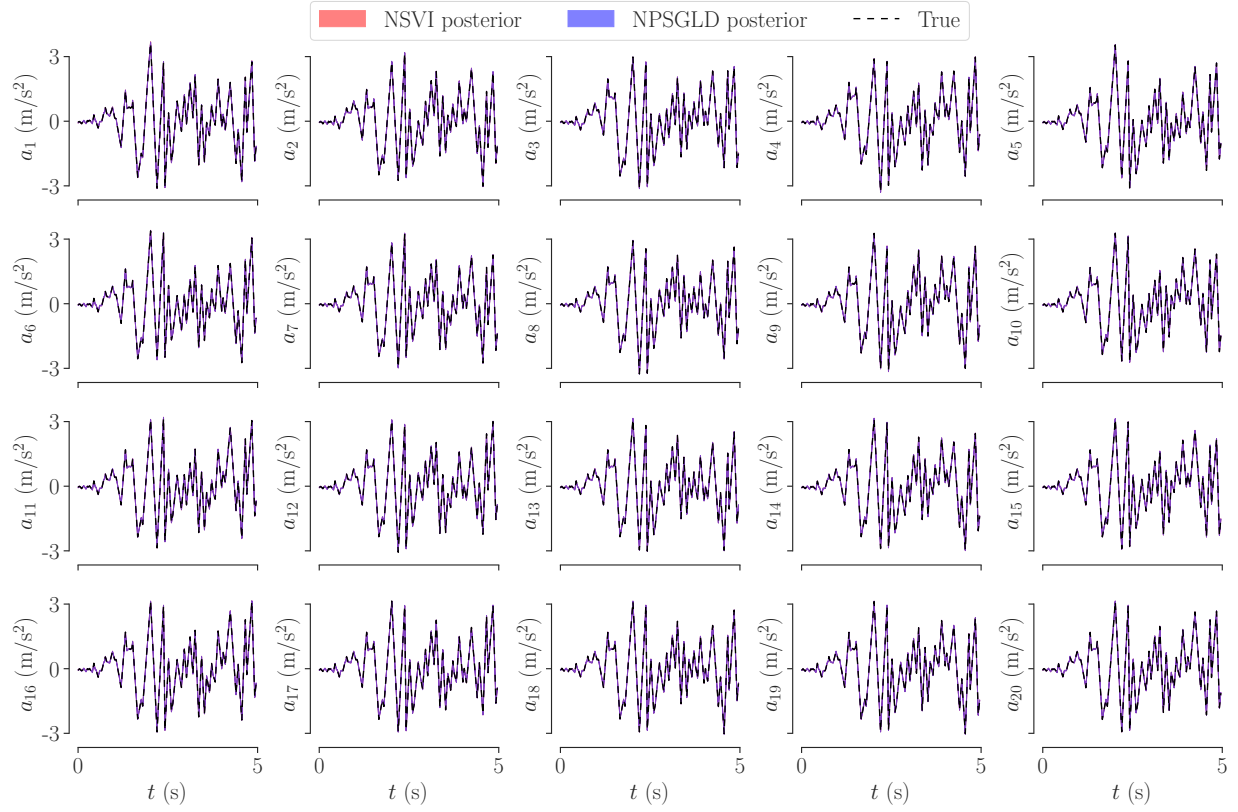


Figure 11: Example of section 5.3: NSVI and NPSGLD posterior distributions of acceleration measurements.

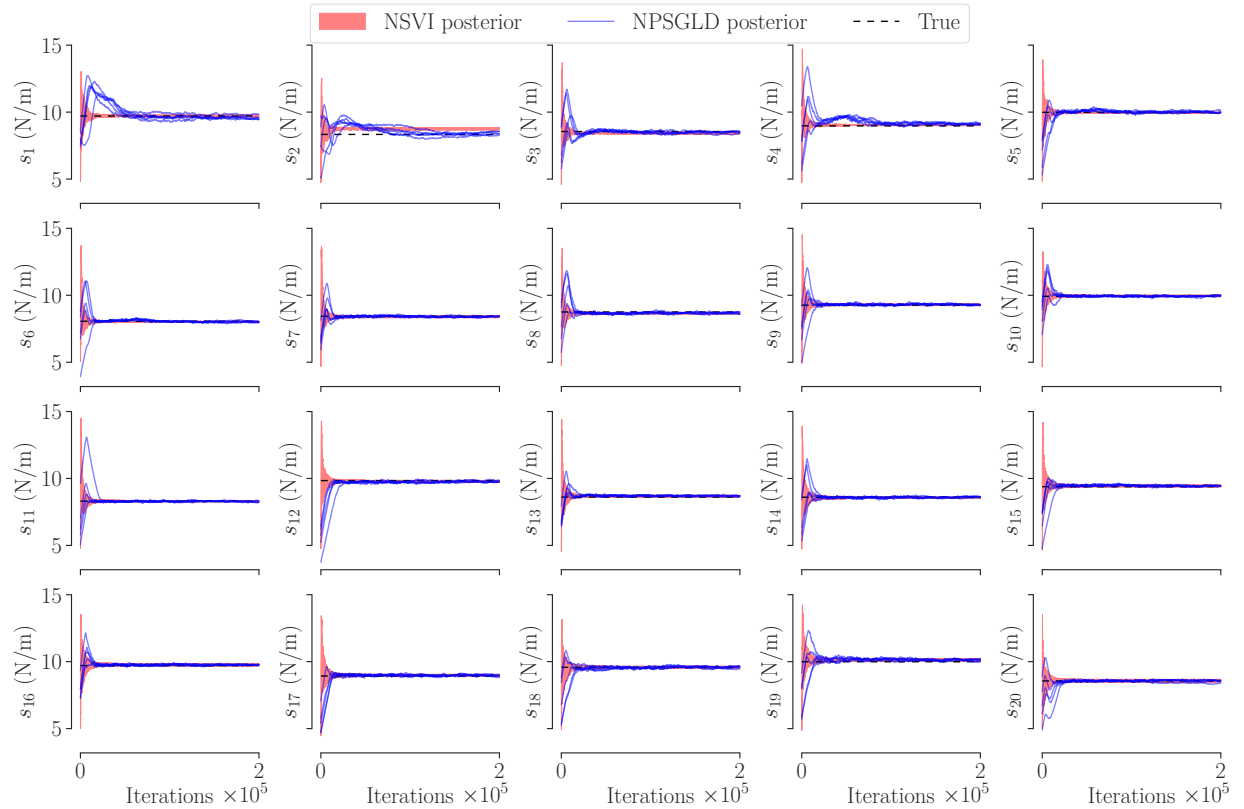


Figure 12: Example of section 5.3: NSVI and NPSGLD convergence speeds of the model parameter posterior.

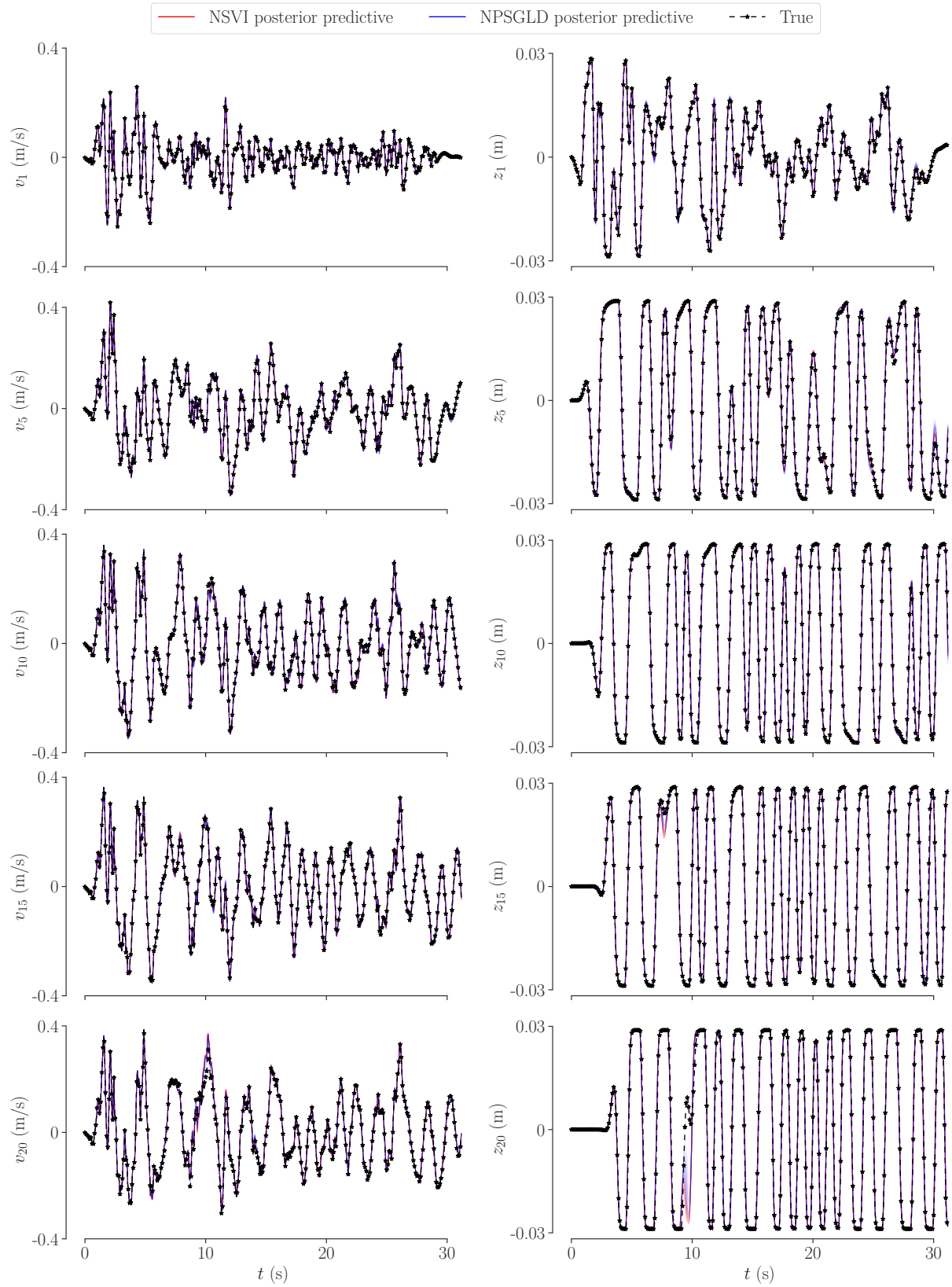


Figure 13: Example of section 5.3: NSVI and NPSGLD posterior predictive distributions.

where $\tanh(200\dot{x})$ is a differentiable approximation of Coulomb damping $\text{sign}\dot{x}$, and \ddot{x}_g is the excitation signal. The mass is known to be 0.664 kg, and the four parameters c_ν , c_f , k and z need to be identified. For more information about the experimental setup and dataset, please refer to section 2 and Table 1 in [Lund et al., 2020].

We follow approach B, proposed by the authors, to process two datasets simultaneously. We achieve this by stacking two independent governing equations using Eq. (11), one governing equation corresponding to one dataset. We use x_1 and x_2 to denote the displacement and velocity of the nonlinear energy sink device in the first experiment, and x_3 and x_4 to denote the counterpart in the second experiment. The two experiments share the same four parameters, so the four-dimensional state space model is:

$$\begin{aligned} \dot{x}_1 &= x_2, & \dot{x}_2 &= -\frac{1}{m} (c_\nu x_2 + c_f \tanh(200x_2) + kx_1 + zx_1^3) - \ddot{x}_{g,1}, \\ \dot{x}_3 &= x_4, & \dot{x}_4 &= -\frac{1}{m} (c_\nu x_4 + c_f \tanh(200x_4) + kx_3 + zx_3^3) - \ddot{x}_{g,2}. \end{aligned}$$

The two measurements are the displacement and relative acceleration of the nonlinear energy sink device:

$$\begin{aligned} y_1 &= x_1, & y_2 &= -\frac{1}{m} (c_\nu x_2 + c_f \tanh(200x_2) + kx_1 + zx_1^3), \\ y_3 &= x_3, & y_4 &= -\frac{1}{m} (c_\nu x_4 + c_f \tanh(200x_4) + kx_3 + zx_3^3). \end{aligned}$$

Since measurement data were collected at 4096 Hz, when running NIFF, we only subsample at these discrete sampling time points to evaluate the physics-informed conditional prior instead of sampling time uniformly as in Eq. (12).

The two training experimental datasets are shown in Fig. 14 using blue color. The left column shows the entire 90-second data. The top two rows are the displacement and acceleration of the nonlinear energy sink under a sine sweep excitation signal with a 5 Hz frequency and a 2.7 mm maximum amplitude. The bottom two rows are the displacements and accelerations under a sine excitation signal with a 5 Hz frequency, and an increasing and decreasing amplitude whose peak is 2.7 mm. Since the signals vary fast, we use 4000 radial basis terms for each signal without using a residual path. We only show the NSVI result as NPSGLD converges extremely slowly, i.e., several hours, for this example due to the significant amount of unknown parameters.

Fig. 14 plots the posterior distributions of displacements and accelerations. As the details of the entire signals on the left column are not visible, we plot the zoom-in region on the right column. The posterior distribution agrees with the measurement data. Fig. 15 plots the posterior distribution of the four model parameters in the bottom row and the convergence speeds in the top row. Our identified parameter values are similar to the results in Tables 2, 3, and 4 of [Lund et al., 2020]. Finally, we check the posterior predictive distributions using four different experimental datasets. Fig. 16 summarizes the prediction results. In the figure, each row corresponds to one experimental dataset. The first column is for displacements and the second column is for accelerations. To account for the posterior predictive randomness, we use and modify the same error analysis metric, normalized mean square error (MSE) indicator [Worden, 1990] used in [Lund et al., 2020]:

$$MSE = \mathbb{E}_{\hat{X}_{1:N}, \hat{\ddot{X}}_{1:N}} \left[\frac{100}{N} \sum_{i=1}^N \left(\frac{(x_i - \hat{X}_i)^2}{\sigma_d^2} + \frac{(\ddot{x}_i - \hat{\ddot{X}}_i)^2}{\sigma_a^2} \right) \right],$$

where $\hat{X}_{1:N}$ and $\hat{\ddot{X}}_{1:N}$ are the posterior predictive displacements and accelerations at N sampling times, x_i and \ddot{x}_i are the measurement data, $\sigma_d^2 = 1.44 \times 10^{-12} \text{ m}^2$ and $\sigma_a^2 = 5.32 \times 10^{-3} (\text{m/s}^2)^2$ are the measurement variances chosen the same values from [Lund et al., 2020]. Table. 1 summarizes the MSE values for the four validation experimental datasets. The magnitudes are similar to the values in Tables 2, 3, and 4 of [Lund et al., 2020].

Table 1: MSE for posterior predictive validation.

	Signal 1	Signal 2	Signal 3	Signal 4
MSE/ 10^8	1.6	16.9	8.1	1.7

6 Conclusions

We have developed the neural information field filter for Bayesian estimation of states and parameters in dynamical systems. NIFF parameterizes the dynamical state path using a residual neural network to improve the parameterization

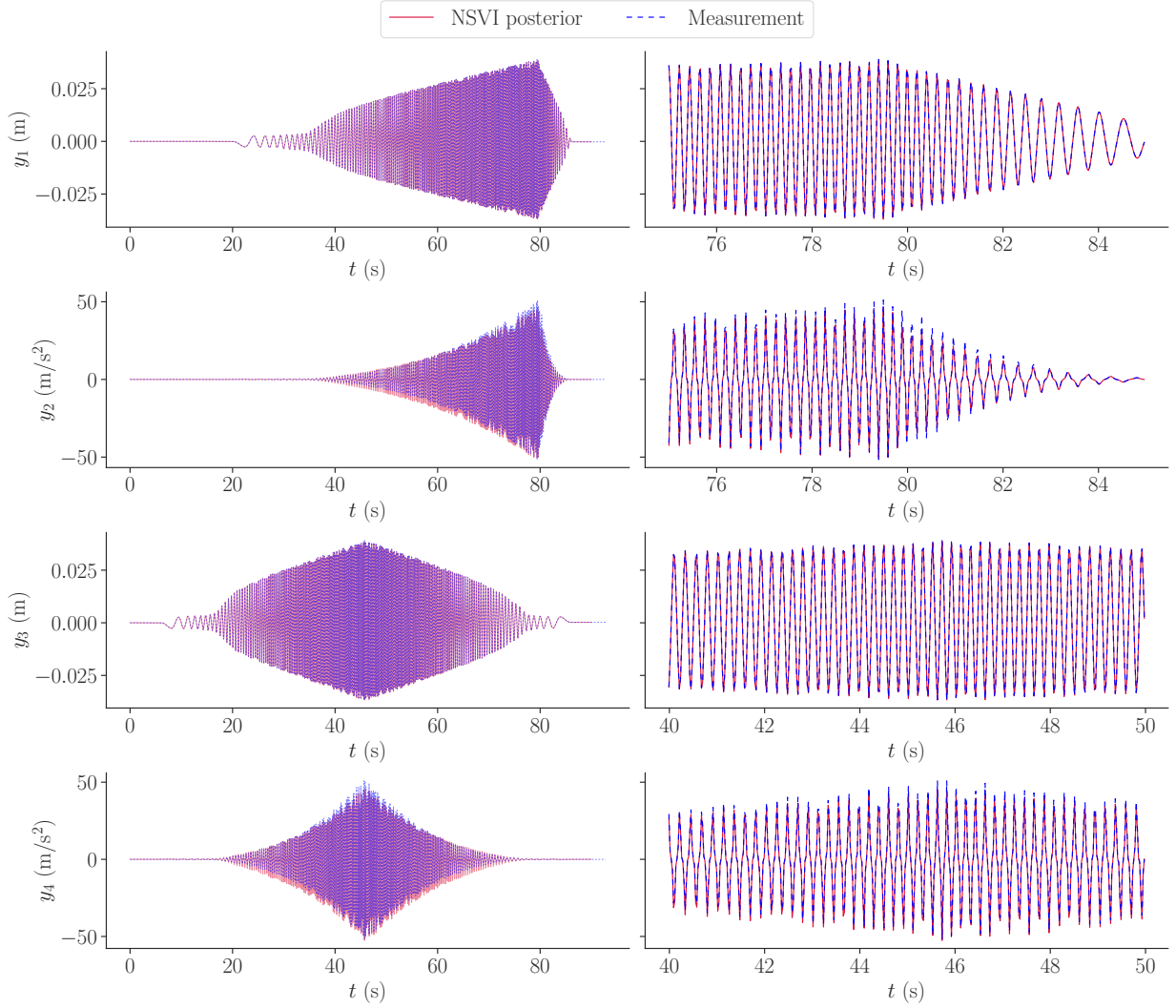


Figure 14: Example of section 5.4: NSVI posterior distribution. The left column includes the entire dataset results, and the right column is zoom-in dataset results.

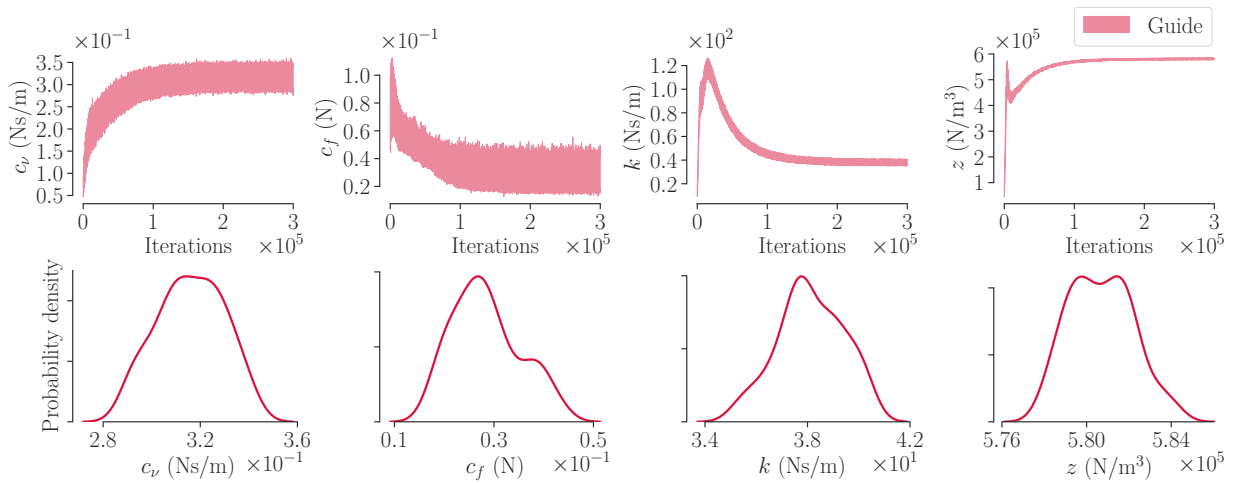


Figure 15: Example of section 5.4: NSVI posterior distribution of model parameters and the convergence speed.

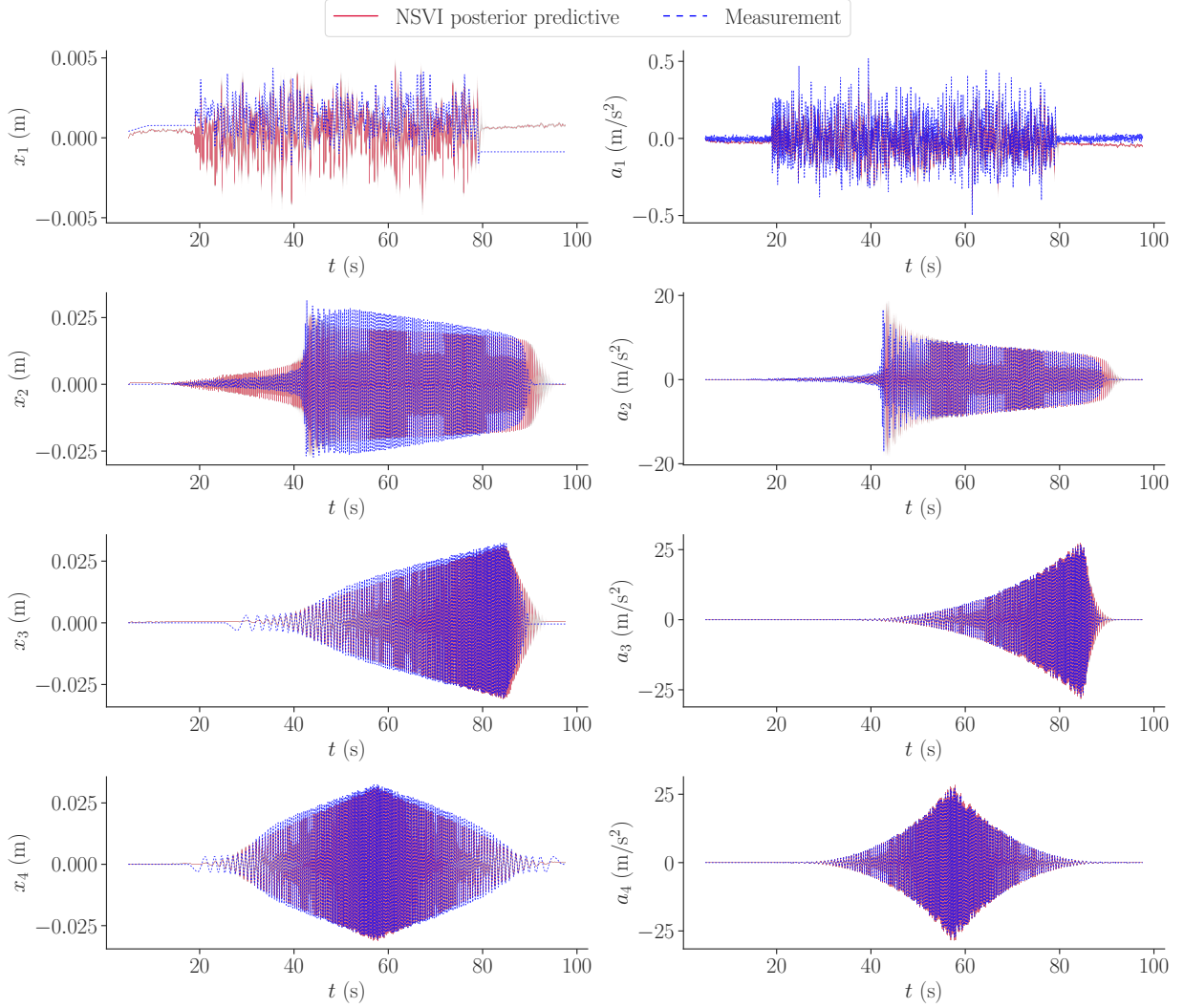


Figure 16: Example of section 5.4: NSVI posterior predictive distribution.

expressiveness and reconstruction accuracy. To this end, we introduced a generalized physics-informed conditional prior by incorporating a kernel information Hamiltonian that measures the similarity between the initial state of the parameterized state path and an auxiliary initial state. We showed the physics-informed conditional prior defined in [Hao and Bilonis, 2024] is a special case of the generalized physics-informed conditional prior when using a Dirac kernel. To sample from the posterior distribution, we developed an optimization algorithm, the nested stochastic variational inference, and a sampling algorithm, the nested preconditioned stochastic gradient Langevin dynamics. We conducted three synthetic examples and one experimental example. In the first example, we studied a single-degree-of-freedom Duffing oscillator. This example aims to compare and verify the proposed non-reparameterized state path function approach in this paper with the reparameterized state path function approach in [Hao and Bilonis, 2024]. We observed that these two formulations produce similar results. In the second example, we studied the improvement by adding a residual function to parameterize the state path function. We used a two-degree-of-freedom nonlinear system considered in [Kong et al., 2022]. We found that adding a residual function can effectively improve the reconstruction accuracy. In the last synthetic example, we demonstrated the performance of NIFF on a twenty-story frame structure model as a high-dimensional problem. Both proposed numerical algorithms show reasonably accurate results. Last, we successfully validate NIFF using a nonlinear energy sink experimental example. In summary, the developed NIFF methodology is a powerful framework for Bayesian estimation in dynamical systems.

Acknowledgments

This work was supported by a Space Technology Research Institutes Grant (number 80NSSC19K1076) from NASA's Space Technology Research Grants Program.

Declaration of generative AI and AI-assisted technologies in the writing process

During the preparation of this work the authors used Grammarly and Chat GPT in order to correct spelling, grammatical, and syntactical errors. After using this tool/service, the authors reviewed and edited the content as needed and take full responsibility for the content of the publication.

A Proof of Proposition 1

Proof. First we show $p(w_{-i}|x_0, \theta) = \tilde{p}(w_{-i}|x_0, \theta)$. From the definition of $p(w|x_0, \theta)$, we have

$$\begin{aligned} p(w|x_0, \theta) &= \frac{e^{-\beta H(w, \theta) - H(\hat{x}(0; w), x_0)}}{\int dw' e^{-\beta H(w', \theta) - H(\hat{x}(0; w'), x_0)}} \\ &= \frac{\delta(w_i - \mathcal{T}(x_0; w_{-i})) e^{-\beta H(w, \theta)}}{\int dw'_{-i} \int dw'_i \delta(w'_i - \mathcal{T}(x_0; w'_{-i})) e^{-\beta H(w', \theta)}} \\ &= \frac{\delta(w_i - \mathcal{T}(x_0; w_{-i})) e^{-\beta H(w, \theta)}}{\int dw'_{-i} e^{-\beta H(w'_{-i}, \mathcal{T}(x_0; w'_{-i}), \theta)}}. \end{aligned}$$

Then, we have

$$\begin{aligned} p(w_{-i}|x_0, \theta) &= \int dw_i p(w|x_0, \theta) \\ &= \int dw_i \frac{\delta(w_i - \mathcal{T}(x_0; w_{-i})) e^{-\beta H(w, \theta)}}{\int dw'_{-i} e^{-\beta H(w'_{-i}, \mathcal{T}(x_0; w'_{-i}), \theta)}} \\ &= \frac{e^{-\beta H(w_{-i}, \mathcal{T}(x_0; w_{-i}), \theta)}}{\int dw'_{-i} e^{-\beta H(w'_{-i}, \mathcal{T}(x_0; w'_{-i}), \theta)}} \\ &= \frac{e^{-\beta \tilde{H}(w_{-i}, x_0, \theta)}}{\int dw'_{-i} e^{-\beta \tilde{H}(w'_{-i}, x_0, \theta)}} \\ &= \tilde{p}(w_{-i}|x_0, \theta). \end{aligned}$$

Next, we show $p(w|\theta) = \tilde{p}(w|\theta)$. We need to use the composition with a function property of the Dirac function [Gel'fand and Vilenkin, 2014], and derive

$$\delta(w_i - \mathcal{T}(x_0; w_{-i})) = \frac{\delta(x_0 - \mathcal{T}^{-1}(w_i; w_{-i}))}{\left| \frac{d\mathcal{T}(x; w_{-i})}{dx} \Big|_{x=\mathcal{T}^{-1}(w_i; w_{-i})} \right|}.$$

We first work on the generalized physics-informed conditional prior.

$$\begin{aligned} p(w|\theta) &= \int dx_0 p(w|x_0, \theta) p(x_0) \\ &= \int dx_0 \frac{\delta(w_i - \mathcal{T}(x_0; w_{-i})) e^{-\beta H(w, \theta)}}{\int dw'_{-i} e^{-\beta H(w'_{-i}, \mathcal{T}(x_0; w'_{-i}), \theta)}} p(x_0) \\ &= \int dx_0 \frac{\delta(x_0 - \mathcal{T}^{-1}(w_i; w_{-i}))}{\left| \frac{d\mathcal{T}(x; w_{-i})}{dx} \Big|_{x=\mathcal{T}^{-1}(w_i; w_{-i})} \right|} \frac{e^{-\beta H(w, \theta)}}{\int dw'_{-i} e^{-\beta H(w'_{-i}, \mathcal{T}(x_0; w'_{-i}), \theta)}} p(x_0) \\ &= \frac{1}{\left| \frac{d\mathcal{T}(x; w_{-i})}{dx} \Big|_{x=\mathcal{T}^{-1}(w_i; w_{-i})} \right|} \frac{e^{-\beta H(w, \theta)}}{\int dw'_{-i} e^{-\beta H(w'_{-i}, \mathcal{T}(\mathcal{T}^{-1}(w_i; w_{-i}); w'_{-i}), \theta)}} p(\mathcal{T}^{-1}(w_i; w_{-i})) \\ &= \frac{1}{\left| \frac{d\mathcal{T}(x; w_{-i})}{dx} \Big|_{x=\hat{x}(0; w)} \right|} \frac{e^{-\beta H(w, \theta)}}{\int dw'_{-i} e^{-\beta H(w'_{-i}, \mathcal{T}(\hat{x}(0; w); w'_{-i}), \theta)}} p(\hat{x}(0; w)). \end{aligned}$$

For the reparameterized version, we have $w_i = \mathcal{T}(x_0; w_{-i})$. Then, we define the map $\mathcal{G} : (w_{-i}, x_0) \mapsto (w_{-i}, \mathcal{T}(x_0; w_{-i}))$.

$$\begin{aligned}
\tilde{p}(w|\theta) &= \left| \nabla_{w_{-i}, w_i} \mathcal{G}^{-1}(w_{-i}, w_i) \right| \tilde{p}(\mathcal{G}^{-1}(w_{-i}, w_i)|\theta) \\
&= \left| \frac{d\mathcal{T}^{-1}(w_i; w_{-i})}{dw_i} \right| \tilde{p}(w_{-i}, \mathcal{T}^{-1}(w_i; w_{-i})|\theta) \\
&= \left| \frac{d\mathcal{T}^{-1}(w_i; w_{-i})}{dw_i} \right| \tilde{p}(w_{-i}|\mathcal{T}^{-1}(w_i; w_{-i}), \theta) p(\mathcal{T}^{-1}(w_i; w_{-i})) \\
&= \frac{1}{\left| \frac{d\mathcal{T}(x; w_{-i})}{dx} \Big|_{x=\mathcal{T}^{-1}(w_i; w_{-i})} \right|} \tilde{p}(w_{-i}|\mathcal{T}^{-1}(w_i; w_{-i}), \theta) p(\mathcal{T}^{-1}(w_i; w_{-i})) \\
&= \frac{1}{\left| \frac{d\mathcal{T}(x; w_{-i})}{dx} \Big|_{x=\mathcal{T}^{-1}(w_i; w_{-i})} \right|} \frac{e^{-\beta \tilde{H}(w_{-i}, \mathcal{T}^{-1}(w_i; w_{-i}), \theta)}}{\int dw'_{-i} e^{-\beta \tilde{H}(w'_{-i}, \mathcal{T}^{-1}(w_i; w_{-i}), \theta)}} p(\mathcal{T}^{-1}(w_i; w_{-i})) \\
&= \frac{1}{\left| \frac{d\mathcal{T}(x; w_{-i})}{dx} \Big|_{x=x_0} \right|} \frac{e^{-\beta H(w_{-i}, w_i, \theta)}}{\int dw'_{-i} e^{-\beta H(w'_{-i}, \mathcal{T}(x_0; w'_{-i}), \theta)}} p(x_0).
\end{aligned}$$

Due to the reparameterization, we have $\hat{x}(0; w) = x_0$. So we have $p(w|\theta) = \tilde{p}(w|\theta)$. \square

B Proposition 2

Proposition 2. *Maximizing the ELBO Eq. (8) is equivalent to minimizing an upper bound of the KL divergence $D_{KL}(q_\phi(w)q_\psi(\theta)||p(w, \theta|y))$.*

Proof. We work with the following compact form of the ELBO:

$$\text{ELBO}(\phi, \psi, \chi|y) = \mathbb{E}_{q_\phi(w)q_\psi(\theta)q_\chi(x_0)} \left[\log \left\{ \frac{p(y|w, \theta)p(w|x_0, \theta)p(x_0, \theta)}{q_\phi(w)q_\psi(\theta)q_\chi(x_0)} \right\} \right].$$

It is easy to see this form is equivalent to Eq. (8).

We decompose the log evidence into three terms:

$$\begin{aligned}
\log p(y) &= \mathbb{E}_{q_\phi(w)q_\psi(\theta)q_\chi(x_0)} [\log p(y)] \\
&= \mathbb{E}_{q_\phi(w)q_\psi(\theta)q_\chi(x_0)} \left[\log \left\{ \frac{p(y, w, \theta, x_0)}{p(w, \theta, x_0|y)} \right\} \right] \\
&= \mathbb{E}_{q_\phi(w)q_\psi(\theta)q_\chi(x_0)} \left[\log \left\{ \frac{p(y, w, \theta, x_0) q_\phi(w)q_\psi(\theta)q_\chi(x_0)}{p(w, \theta, x_0|y) q_\phi(w)q_\psi(\theta)q_\chi(x_0)} \right\} \right] \\
&= \mathbb{E}_{q_\phi(w)q_\psi(\theta)q_\chi(x_0)} \left[\log \left\{ \frac{q_\phi(w)q_\psi(\theta)q_\chi(x_0)}{p(w, \theta, x_0|y)} \right\} \right] + \mathbb{E}_{q_\phi(w)q_\psi(\theta)q_\chi(x_0)} \left[\log \left\{ \frac{p(y, w, \theta, x_0)}{q_\phi(w)q_\psi(\theta)q_\chi(x_0)} \right\} \right] \\
&= \mathbb{E}_{q_\phi(w)q_\psi(\theta)} \left[\log \left\{ \frac{q_\phi(w)q_\psi(\theta)}{p(w, \theta|y)} \right\} \right] + \mathbb{E}_{q_\phi(w)q_\psi(\theta)q_\chi(x_0)} \left[\log \left\{ \frac{q(x_0)}{p(x_0|w, \theta, y)} \right\} \right] + \text{ELBO}(\phi, \psi, \chi|y) \\
&= \text{KL} [q_\phi(w)q_\psi(\theta)||p(w, \theta|y)] + \mathbb{E}_{q_\phi(w)q_\psi(\theta)} [\text{KL} [q(x_0)||p(x_0|w, \theta, y)]] + \text{ELBO}(\phi, \psi, \chi|y).
\end{aligned}$$

Since $\log p(y)$ is a constant, and $\mathbb{E}_{q_\phi(w)q_\psi(\theta)} [\text{KL} [q(x_0)||p(x_0|w, \theta, y)]]$ is non-negative, we conclude the equivalence. \square

C NSVI implementation details

We write the information Hamiltonian $H_1(w, \theta)$ using expectation, so it can be estimated using Monte Carlo methods. Let

$$h_1(w, \theta, t) = \|\dot{\hat{x}}(t; w) - f(\hat{x}(t; w), t; \theta)\|^2,$$

and t follow the uniform distribution $p(t) = \mathcal{U}([0, T])$, we write

$$H_1(w, \theta) = T \mathbb{E}_{p(t)} [h_1(w, \theta, t)].$$

So the log unnormalized relaxed physics-informed conditional prior is

$$\log \pi(w|x_0, \theta) = -\beta_1 T \mathbb{E}_{p(t)} [h_1(w, \theta, t)] - \beta_2 H_2(\hat{x}(0; w), x_0). \quad (12)$$

Algorithm 1: SVI approximation to $p(w|x_0, \theta)$.

SVI_PRIOR: (

x_0 , # The auxiliary initial state.
 θ , # Model parameter.
 ϕ , # Initial variational parameter.
niter, # The number of optimization iterations.
 $(n_{\bar{\epsilon}}, n_{\bar{t}})$, # Sample sizes.

)

for $it = 0; it < niter; it = it + 1$ **do**

 Sample ϵ_i independently from $q(\epsilon)$;
 Sample t_{ij} independently from $\mathcal{U}([0, T])$;
 Compute $\nabla_{\phi} \widehat{\text{ELBO}}(\phi|x_0, \theta)$ using Eq. (13) ;
 Update ϕ using Adam with the gradient estimate $\nabla_{\phi} \widehat{\text{ELBO}}(\phi|x_0, \theta)$.

end

Return: ϕ # Final variational parameters.

C.1 SVI to approximate the relaxed physics-informed conditional prior $p(w|x_0, \theta)$

We first describe the inner loop auxiliary stochastic variational inference. We parameterize the guide $q_{\phi}(w)$ with the parameter ϕ to approximate the relaxed physics-informed conditional prior $p(w|x_0, \theta)$ by maximizing the prior ELBO:

$$\text{ELBO}(\phi|x_0, \theta) = \mathbb{E}_{q_{\phi}(w)} \left[\log \frac{\pi(w|x_0, \theta)}{q_{\phi}(w)} \right].$$

The log unnormalized relaxed physics-informed conditional prior is defined in Eq. (12).

Applying Eq. (12), the equivalent prior ELBO is

$$\text{ELBO}(\phi|x_0, \theta) = \mathbb{E}_{q_{\phi}(w)p(t)} [-T\beta_1 h(w, \theta, t) - \beta_2 H_2(\hat{x}(0; w), x_0) - \log q_{\phi}(w)].$$

Maximizing the prior ELBO requires computing its gradient with respect to the variational parameter ϕ . We apply the reparameterization trick [Kingma and Welling, 2013]. Specifically, we choose a base distribution $q(\epsilon)$ and a deterministic transformation g_{ϕ} parameterized by the same variational parameter ϕ such that $g_{\phi}(\epsilon) \sim q_{\phi}$. For more details, refer to section 2.4.4 in [Hao and Bilonis, 2024]. Then the reparameterized ELBO is

$$\text{ELBO}(\phi|x_0, \theta) = \mathbb{E}_{q(\epsilon)p(t)} [-T\beta_1 h(g_{\phi}(\epsilon), \theta, t) - \beta_2 H_2(\hat{x}(0; g_{\phi}(\epsilon)), x_0) - \log q_{\phi}(g_{\phi}(\epsilon))]$$

Its gradient with respect to the variational parameter ϕ is

$$\nabla_{\phi} \text{ELBO}(\phi|x_0, \theta) = \mathbb{E}_{q(\epsilon)p(t)} [\nabla_{\phi} [-T\beta_1 h(g_{\phi}(\epsilon), \theta, t) - \beta_2 H_2(\hat{x}(0; g_{\phi}(\epsilon)), x_0) - \log q_{\phi}(g_{\phi}(\epsilon))]].$$

Let ϵ_i and t_{ij} be the random samples from $q(\epsilon)$ and $p(t)$, an unbiased estimator of this gradient is

$$\nabla_{\phi} \widehat{\text{ELBO}}(\phi|x_0, \theta) = \frac{1}{N_{\epsilon} N_t} \sum_{i=1}^{N_{\epsilon}} \sum_{j=1}^{N_t} \nabla_{\phi} [-T\beta_1 h(g_{\phi}(\epsilon_i), \theta, t_{ij}) - \beta_2 H_2(\hat{x}(0; g_{\phi}(\epsilon_i)), x_0) - \log q_{\phi}(g_{\phi}(\epsilon_i))]. \quad (13)$$

We summarize the algorithm in Algorithm 1.

C.2 NSVI to approximate the marginal posterior $p(w, \theta|y)$

As before, we apply the reparameterization trick to the ELBO defined in Eq. (8). Let $(q(\epsilon), q(\eta), q(\zeta))$ be the base distributions and $(g_{\phi}, g_{\psi}, g_{\eta})$ be the corresponding deterministic transformations such that $g_{\phi}(\epsilon) \sim q_{\phi}$, $g_{\psi}(\eta) \sim q_{\psi}$, and $g_{\chi}(\zeta) \sim q_{\chi}$. Then, the reparameterized ELBO is

$$\begin{aligned} \text{ELBO}(\phi, \psi, \chi|y) = & + \mathbb{E}_{q(\epsilon)q(\eta)p(\mathcal{I}_{m_d})} \left[\frac{n_d}{m_d} \sum_{i \in \mathcal{I}_{m_d}} \log p(y_i | g_{\phi}(\epsilon), g_{\psi}(\eta)) \right] \\ & + \mathbb{E}_{q(\epsilon)q(\eta)q(\zeta)} [\log \pi(g_{\phi}(\epsilon) | g_{\chi}(\zeta), g_{\psi}(\eta))] \\ & + \mathbb{E}_{q(\eta)q(\zeta)} [\log p(g_{\chi}(\zeta), g_{\psi}(\eta))] \\ & - \mathbb{E}_{q(\epsilon)q(\eta)q(\zeta)} [\log q_{\phi}(g_{\phi}(\epsilon)) q_{\psi}(g_{\psi}(\eta)) q_{\chi}(g_{\chi}(\zeta))] \\ & - \mathbb{E}_{q(\eta)q(\zeta)} [\log Z(g_{\chi}(\zeta), g_{\psi}(\eta))] \end{aligned} \quad (14)$$

Taking the ELBO’s gradient requires to differentiate through the log partition function, which has the formula [Hao and Bilonis, 2024]:

$$\nabla_{\psi, \chi} \log Z(g_\chi(\zeta), g_\psi(\eta)) = \mathbb{E}_{p(\tilde{w}|g_\chi(\zeta), g_\psi(\eta))} [\nabla_{\psi, \chi} \log [\pi(\tilde{w}|g_\chi(\zeta), g_\psi(\eta))]]. \quad (15)$$

To evaluate it, we need to sample from the relaxed physics-informed conditional prior $p(\tilde{w}|g_\chi(\zeta), g_\psi(\eta))$. We will use Algorithm 1 to build a surrogate sampler.

Applying Eq. (12) to Eq. (15) and substitute the result into the ELBO Eq. (14), the gradient of ELBO is

$$\begin{aligned} \nabla_{\phi, \psi, \chi} \text{ELBO}(\phi, \psi, \chi|y) = & + \mathbb{E}_{q(\epsilon)q(\eta)p(\mathcal{I}_{m_d})} \left[\frac{n_d}{m_d} \sum_{i \in \mathcal{I}_{m_d}} \nabla_{\phi, \psi} \log p(y_i|g_\phi(\epsilon), g_\psi(\eta)) \right] \\ & - \mathbb{E}_{q(\epsilon)q(\eta)q(\zeta)p(t)} [\nabla_{\phi, \psi, \chi} [T\beta_1 h(g_\phi(\epsilon), g_\psi(\eta), t) + \beta_2 H_2(\hat{x}(0); g_\phi(\epsilon), g_\chi(\zeta))] \\ & + \mathbb{E}_{q(\eta)q(\zeta)} [\nabla_{\psi, \chi} \log p(g_\chi(\zeta), g_\psi(\eta))] \\ & - \mathbb{E}_{q(\epsilon)q(\eta)q(\zeta)} [\nabla_{\phi, \psi, \chi} \log q_\phi(g_\phi(\epsilon))q_\psi(g_\psi(\eta))q_\chi(g_\chi(\zeta))] \\ & + \mathbb{E}_{q(\eta)q(\zeta)p(\tilde{w}|g_\chi(\zeta), g_\psi(\eta))p(\tilde{t})} [\nabla_{\psi, \chi} [T\beta_1 h(\tilde{w}, g_\psi(\eta), \tilde{t}) + \beta_2 H_2(\hat{x}(0); \tilde{w}, g_\chi(\zeta))] \end{aligned}$$

To build an unbiased estimator for the ELBO’s gradient, we sample $(\epsilon_i, \eta_i, \zeta_i)$ from $(q(\epsilon), q(\eta), q(\zeta))$, t_{ij} from $p(t)$, \tilde{w}_{ik} from $p(\tilde{w}|g_\chi(\zeta_i), g_\psi(\eta_i))$, \tilde{t}_{ikl} from $p(\tilde{t})$, and only subsample one dataset with the index set I_{m_d} to get

$$\begin{aligned} \nabla_{\phi, \psi, \chi} \widehat{\text{ELBO}}(\phi, \psi, \chi|y) = & + \frac{n_d}{N_{\epsilon\eta\zeta} m_d} \sum_{i=1}^{N_{\epsilon\eta\zeta}} \sum_{n \in I_{m_d}} \nabla_{\phi, \psi} \log p(y_n|g_\phi(\epsilon_i), g_\psi(\eta_i)) \\ & - \frac{1}{N_{\epsilon\eta\zeta} N_t} \sum_{i=1}^{N_{\epsilon\eta\zeta}} \sum_{j=1}^{N_t} \nabla_{\phi, \psi, \chi} [T\beta_1 h(g_\phi(\epsilon_i), g_\psi(\eta_i), t_{ij}) + \beta_2 H_2(\hat{x}(0); g_\phi(\epsilon_i), g_\chi(\zeta_i))] \\ & + \frac{1}{N_{\epsilon\eta\zeta}} \sum_{i=1}^{N_{\epsilon\eta\zeta}} \nabla_{\psi, \chi} \log p(g_\chi(\zeta_i), g_\psi(\eta_i)) \\ & - \frac{1}{N_{\epsilon\eta\zeta}} \sum_{i=1}^{N_{\epsilon\eta\zeta}} \nabla_{\phi, \psi, \chi} \log [q_\phi(g_\phi(\epsilon_i))q_\psi(g_\psi(\eta_i))q_\chi(g_\chi(\zeta_i))] \\ & + \frac{1}{N_{\epsilon\eta\zeta} N_{\tilde{w}} N_{\tilde{t}}} \sum_{i=1}^{N_{\epsilon\eta\zeta}} \sum_{k=1}^{N_{\tilde{w}}} \sum_{l=1}^{N_{\tilde{t}}} \nabla_{\psi, \chi} [T\beta_1 h(\tilde{w}_{ik}, g_\psi(\eta_i), \tilde{t}_{ikl}) + \beta_2 H_2(\hat{x}(0); \tilde{w}_{ik}, g_\chi(\zeta_i))] \end{aligned} \quad (16)$$

To compute this estimator, we have to draw \tilde{w}_{ik} from the relaxed physics-informed conditional prior $p(\tilde{w}|g_\chi(\zeta_i), g_\psi(\eta_i))$. We run Algorithm 1 to get surrogate samples using the optimized guide $q_{\tilde{w}_i}(\tilde{w})$. We call this inner loop auxiliary stochastic variational inference. For the computational efficiency purpose, we only draw one sample from $q(\epsilon)$, $q(\eta)$, and $q(\zeta)$, i.e., $N_{\epsilon\eta\zeta} = 1$. Moreover, we run Algorithm 1 in a non-convergent and persistent manner. This means that we do not run the inner loop auxiliary algorithm until convergence. Instead, we only update a few steps, e.g., ten steps, and initialize the inner loop auxiliary algorithm at the next optimization iteration using the trained auxiliary guide parameter at the current iteration step.

Algorithm 2 summarizes the steps to approximate the marginal posterior distribution.

D NPSGLD implementation details

From our numerical experiments, the adaptively-updated rules in Eqs. (19) and (22) generally speed up the convergence speed at the initial phase of MCMC sampling when larger updated step sizes are desired. However, it results in an instability issue when MC chains have traveled to the target probability density modes when small and stable updated step sizes are desired. To resolve this issue, we gradually anneal the memorizing size parameter α to 1. Numerically, we create a monotonically increasing vector α , which anneals the memorizing size parameter during a user-specified number of iterations. So, we adaptively precondition the SGLD at the initial sampling phase to accelerate the MC chains traversing in the space. The SGLD is statically preconditioned when $\alpha = 1$, which stabilizes the MC chains once they are in target density modes.

Algorithm 2: NSVI approximation to $p(w, \theta|y)$.

NSVI_POSTERIOR: (

$(\phi, \psi, \chi, \tilde{\phi})$, # Variational parameters.
 (niter, niter_auxi), # The number of optimization iterations.
 $(n_{\epsilon\eta\zeta}, n_t, \tilde{n}_\epsilon, \tilde{n}_t, m_y)$, # Sample sizes.

)

for $it = 0; it < niter; it = it + 1$ **do**

 Sample $(\epsilon_1, \eta_1, \zeta_1) \sim q$, # Assuming $n_{\epsilon\eta\zeta} = 1$ for computational efficiency.

 Compute $(\theta_1, x_{0,1}) = (g_\psi(\eta_1), g_\chi(\zeta_1))$;

$\tilde{\phi} \leftarrow \text{SVI_PRIOR}(x_{0,1}, \theta_1, \tilde{\phi}, \text{niter_auxi}, (\tilde{n}_\epsilon, \tilde{n}_t))$, # Run **Algorithm 1**.

 Sample \tilde{w}_{1k} independently from $q_{\tilde{\phi}}$;

 Sample t_{1j} independently from $\mathcal{U}([0, T])$;

 Sample \tilde{t}_{1kl} independently from $\mathcal{U}([0, T])$;

 Compute $\nabla_{\phi, \psi, \chi} \widehat{\text{ELBO}}(\phi, \psi, \chi|y)$ using Eq. (16);

 Update (ϕ, ψ, χ) using Adam with the gradient estimate $\nabla_{\phi, \psi, \chi} \widehat{\text{ELBO}}(\phi, \psi, \chi|y)$.

end

Return: $(q_\phi(w), q_\psi(\theta))$ # Approximate marginal posterior distribution.

D.1 PSGLD to sample from the relaxed physics-informed conditional prior $p(w|x_0, \theta)$

We use PSGLD to sample from the relaxed physics-informed conditional prior $p(w|x_0, \theta)$. The update step is

$$\Delta w_k = \rho_k [M(w_k) \nabla_w \log \pi(w_k|x_0, \theta) + \Gamma(w_k)] + M(w_k)^{\frac{1}{2}} \sqrt{2\rho_k} \xi_k, \quad (17)$$

where, recall from Eq. (12)

$$\nabla_w \log \pi(w_k|x_0, \theta) = -T\beta_1 \mathbb{E}_{t \sim \mathcal{U}([0, T])} [\nabla_w h(w_k, \theta, t)] - \beta_2 \nabla_w H_2(\hat{x}(0; w_k), x_0).$$

We use an unbiased estimator for it:

$$\nabla_w \log \widehat{\pi}(w_k|x_0, \theta) = \frac{-T\beta_1}{n_t} \sum_{i=1}^{n_t} \nabla_w h(w_k, \theta, t_i) - \beta_2 \nabla_w H_2(\hat{x}(0; w_k), x_0). \quad (18)$$

The precondition matrix $M(w_k)$ update rule is

$$\begin{aligned} V(w_k) &= \alpha V(w_{k-1}) + (1 - \alpha) g(w_k) \odot g(w_k), \\ M(w_k) &= \text{diag} \left(\frac{1}{\delta + \sqrt{V(w_k)}} \right), \end{aligned} \quad (19)$$

where

$$g(w_k) = \nabla_w \log \widehat{\pi}(w_k|x_0, \theta).$$

We summarize these steps in Algorithm 3.

D.2 NPSGLD to sample from the marginal posterior $p(w, \theta|y)$

The update rule in Eq. (9) requires taking the gradient of $\log Z(x_{0,k}, \theta_k)$. Similar to the NSVI case, the gradient is

$$\nabla_{\theta, x_0} \log Z(x_{0,k}, \theta_k) = \mathbb{E}_{p(\tilde{w}|x_{0,k}, \theta_k)} [\nabla_{\theta, x_0} \log [\pi(\tilde{w}|x_{0,k}, \theta_k)]] .$$

So the gradient of log relaxed physics-informed conditional prior is

$$\nabla_{w, \theta, x_0} \log p(w_k|x_{0,k}, \theta_k) = \nabla_{w, \theta, x_0} \log \pi(w_k|x_{0,k}, \theta_k) - \mathbb{E}_{p(\tilde{w}|x_{0,k}, \theta_k)} [\nabla_{\theta, x_0} \log [\pi(\tilde{w}|x_{0,k}, \theta_k)]] \quad (20)$$

Algorithm 3: PSGLD to sample from $p(w|x_0, \theta)$.

PSGLD_PRIOR: (

w_0 , # MC chain initial state.
 (x_0, θ) , # the auxiliary initial state and model parameter.
 $niter$, # The number of MC iterations.
 n_t , # Sample size.
 ρ , # Step size.
 (α, δ) , # RMSprop parameters.
 (V, M) , # Initial RMSprop matrices.

)

for $k = 0; k < niter; k = k + 1$ **do**

 Sample t_i independently from $\mathcal{U}([0, T])$;

 Compute $\nabla_w \log \widehat{\pi}(w_k|x_0, \theta)$ using Eq. (18) ;

 Choose the current memorizing size α from α . Update $V(w_k)$ and $M(w_k)$ using Eq. (19) ;

 Compute Δw_k using Eq. (17) and update w_{k+1} .

end

Return: (w_{-1}, V, M) # The final state of MC chain and RMSprop parameters.

We apply Eq. (12) to Eq. (20), and sample t_l from $p(t)$, \tilde{w}_m from $p(\tilde{w}|x_{0,k}, \theta_k)$, and \tilde{t}_{mn} from $p(\tilde{t})$ to get the estimator

$$\begin{aligned} \nabla_{w, \theta, x_0} \log \widehat{\pi}(w_k|x_{0,k}, \theta_k) = & -\frac{T\beta_1}{n_t} \sum_{l=1}^{n_t} \nabla_{w, \theta} h(w_k, \theta_k, t_l) - \beta_2 \nabla_{w, x_0} H_2(\hat{x}(0; w_k), x_{0,k}) \\ & + \frac{T\beta_1}{n_{\tilde{w}} n_{\tilde{t}}} \sum_{m=1}^{n_{\tilde{w}}} \sum_{n=1}^{n_{\tilde{t}}} [\nabla_{\theta} h(\tilde{w}_m, \theta_k, \tilde{t}_{mn}) + \beta_2 \nabla_{x_0} H_2(\hat{x}(0; \tilde{w}_m), x_{0,k})] \end{aligned} \quad (21)$$

The precondition matrix is

$$\begin{aligned} V(w_k, \theta_k, x_{0,k}) &= \alpha V(w_{k-1}, \theta_{k-1}, x_{0,k-1}) + (1 - \alpha) g(w_k, \theta_k, x_{0,k}) \odot g(w_k, \theta_k, x_{0,k}), \\ M(w_k, \theta_k, x_{0,k}) &= \text{diag} \left(\frac{1}{\delta + \sqrt{V(w_k, \theta_k, x_{0,k})}} \right). \end{aligned} \quad (22)$$

In the above equation, we define

$$g(w_k, \theta_k, x_{0,k}) = \frac{n_y}{m_y} \sum_{i=0}^{m_y} \nabla_{w, \theta, x_0} \log p(y_i|w_k, \theta_k) + \nabla_{w, \theta, x_0} \log \widehat{\pi}(w_k|x_{0,k}, \theta_k) + \nabla_{\theta, x_0} \log p(x_{0,k}, \theta_k). \quad (23)$$

Similar to NSVI, we have to sample from the relaxed physics-informed conditional prior $p(\tilde{w}|x_{0,k}, \theta_k)$ to get samples \tilde{w}_m . We use Algorithm 3 to sample from it using another MCMC chain (auxiliary chain). This means that we only consider the case of $n_{\tilde{w}} = 1$.

To improve the computational efficiency, we run NPSGLD in a persistent, short-run, non-convergent manner for the auxiliary chain. Namely, we initialize the auxiliary chain at the next iteration using the result from the current iteration and only update it in several steps, e.g., ten steps. Algorithm 4 outlines the process.

E State filtering

Algorithms 2 and 4 solve the more challenging joint state and parameter estimation problem. If the goal is state filtering only when model parameters are provided, we still apply the two algorithms. We just update the guide or MC chains for the state path parameterization w . The two algorithms do not include the inner loop updates *SVI_PRIOR* and *PSGLD_PRIOR*.

F Computational time

Tables 2, 3, 4 and 5 summarize the dimension of w in $\hat{x}(t; w)$ and computational time for all experiments. In general, we find NSVI is faster than NPSGLD, albeit less accurate than NPSGLD.

Algorithm 4: NPSGLD to sample from $p(w, \theta|y)$.

NPSGLD_POSTERIOR: (

$(w_0, x_{0,0}, \theta_0)$, # MC chain initial states.
 \tilde{w}_0 , # Auxiliary MC chain initial state.
 $(niter, niter_auxi)$, # The number of (auxiliary) MC iterations.
 $(n_t, n_{\tilde{t}}, n_{\tilde{w}}, m_y)$ # Sample size.
 $(\rho, \tilde{\rho})$, # Step size.
 $(\alpha, \delta, \tilde{\alpha}, \tilde{\delta})$, # RMSprop parameters.
 $(V, M, \tilde{V}, \tilde{M})$, # Initial RMSprop matrices.

)

for $k = 0; k < niter; k = k + 1$ **do**

Assuming $n_{\tilde{w}} = 1$ for computational efficiency.

Choose the current memorizing size $\tilde{\alpha}$ from $\tilde{\alpha}$;

$(\tilde{w}_0, \tilde{V}, \tilde{M}) \leftarrow \text{PSGLD_PRIOR}(\tilde{w}_0, (x_{0,k}, \theta_k), niter_auxi, n_{\tilde{t}}, \tilde{\rho}, (\tilde{\alpha}, \tilde{\delta}), (\tilde{V}, \tilde{M}))$, # Run **Algorithm 3**.

Sample t_l and t_{1m} independently from $\mathcal{U}([0, T])$;

Compute $\nabla_{w, \theta, x_0} \log p(w_k | \theta_k, x_{0,k})$ using Eq. (21) with $\tilde{w}_m = \tilde{w}_0$;

Subsample a minibatch dataset $y_{i \in I_{m_d}}$ from y ;

Choose the current memorizing size α from α . Update $V(w_k, \theta_k, x_{0,k})$ and $M(w_k, \theta_k, x_{0,k})$ using Eqs. (22) ;

Compute $(\Delta w_k, \Delta \theta_k, \Delta x_{0,k})$ using Eq. (9) and update $(w_{k+1}, \theta_{k+1}, x_{0,k+1})$.

end

Return: $(w_{1:k}, x_{0,1:k}, \theta_{1:k})$ # MC samples.

Table 2: section 5.1.

	Repara NSVI	Relaxed NSVI	Relaxed NSGLD	Relaxed NPSGLD
w dimension	162	162	162	162
Computational time (s)	8	7	77	90

Table 3: section 5.2.

	w/o residual path: NSVI	w/o residual path: NPSGLD	w/ residual path: NSVI	w/ residual path: NPSGLD
w dimension	80	80	344	344
Computational time (s)	5	25	26	195

Table 4: section 5.3.

	NSVI	NPSGLD
w dimension	4660	4660
Computational time (s)	196	325

Table 5: section 5.4.

	NSVI
w dimension	16000
Computational time (s)	827

References

- Alana Lund, Shirley J Dyke, Wei Song, and Ilias Billionis. Identification of an experimental nonlinear energy sink device using the unscented kalman filter. *Mechanical Systems and Signal Processing*, 136:106512, 2020.
- Tanmoy Chatterjee, Alexander D Shaw, Michael I Friswell, and Hamed Haddad Khodaparast. Sparse bayesian machine learning for the interpretable identification of nonlinear structural dynamics: Towards the experimental data-driven

- discovery of a quasi zero stiffness device. *Mechanical Systems and Signal Processing*, 205:110858, 2023.
- R Nayek, AB Abdessalem, N Dervilis, EJ Cross, and K Worden. Identification of piecewise-linear mechanical oscillators via bayesian model selection and parameter estimation. *Mechanical Systems and Signal Processing*, 196:110300, 2023.
- Rongpeng Li, Supei Zheng, Fengdan Wang, Qingtian Deng, Xinbo Li, Yuzhu Xiao, and Xueli Song. A robust sparse bayesian learning method for the structural damage identification by a mixture of gaussians. *Mechanical Systems and Signal Processing*, 200:110483, 2023.
- Akshay J Thomas, Eduardo Barocio, Ilias Bilonis, and R Byron Pipes. Bayesian inference of fiber orientation and polymer properties in short fiber-reinforced polymer composites. *Composites Science and Technology*, 228:109630, 2022.
- Andres Beltran-Pulido, Dionysios Aliprantis, Ilias Bilonis, Alfredo R Munoz, Franco Leonardi, and Seth M Avery. Uncertainty quantification and sensitivity analysis in a nonlinear finite-element model of a permanent magnet synchronous machine. *IEEE Transactions on Energy Conversion*, 35(4):2152–2161, 2020.
- Zhe Song, Zijun Zhang, Yu Jiang, and Jin Zhu. Wind turbine health state monitoring based on a bayesian data-driven approach. *Renewable energy*, 125:172–181, 2018.
- Antonina M Kosikova, Omid Sedehi, Costas Papadimitriou, and Lambros S Katafygiotis. Bayesian structural identification using gaussian process discrepancy models. *Computer Methods in Applied Mechanics and Engineering*, 417:116357, 2023.
- Dong Hyuk Yi and Cheol Soo Park. Model selection for parameter identifiability problem in bayesian inference of building energy model. *Energy and Buildings*, 245:111059, 2021.
- Kairui Hao, Atharva Hans, Sayantan Bhattacharya, Ilias Bilonis, and Pavlos Vlachos. Unbalanced optimal transport for particle tracking in pvt. *Bulletin of the American Physical Society*, 2023.
- Kairui Hao, Atharva Hans, Pavlos Vlachos, and Ilias Bilonis. Unbalanced optimal transport for stochastic particle tracking. *arXiv preprint arXiv:2407.04583*, 2024.
- Atharva Hans, Sayantan Bhattacharya, Kairui Hao, Pavlos Vlachos, and Ilias Bilonis. Bayesian reconstruction of 3d particle positions in high-seeding density flows. *Measurement Science and Technology*, 2024. URL <http://iopscience.iop.org/article/10.1088/1361-6501/ad6624>.
- Kairui Hao. Comparing the economic performance of ice storage and batteries for buildings with on-site pv through model predictive control. Master’s thesis, Purdue University, 2020.
- Kairui Hao, Donghun Kim, and James E Braun. Comparing the economic performance of ice storage and batteries for buildings with on-site pv through model predictive control and optimal sizing. *Journal of Building Performance Simulation*, 15(5):691–715, 2022.
- Rudolph Emil Kalman. A new approach to linear filtering and prediction problems. 1960.
- Eric A Wan and Rudolph Van Der Merwe. The unscented kalman filter for nonlinear estimation. In *Proceedings of the IEEE 2000 Adaptive Systems for Signal Processing, Communications, and Control Symposium (Cat. No. 00EX373)*, pages 153–158. Ieee, 2000.
- Geir Evensen. The ensemble kalman filter: Theoretical formulation and practical implementation. *Ocean dynamics*, 53:343–367, 2003.
- Brian DO Anderson and John B Moore. *Optimal filtering*. Courier Corporation, 2012.
- Jun S Liu and Rong Chen. Sequential monte carlo methods for dynamic systems. *Journal of the American statistical association*, 93(443):1032–1044, 1998.
- Arnaud Doucet et al. *Sequential Monte Carlo methods in practice*, volume 1. Springer.
- Arnaud Doucet, Simon Godsill, and Christophe Andrieu. On sequential monte carlo sampling methods for bayesian filtering. *Statistics and computing*, 10:197–208, 2000.
- Alana Lund, Ilias Bilonis, and Shirley J Dyke. Variational inference for nonlinear structural identification. *Journal of Applied and Computational Mechanics*, 7(Special Issue):1218–1231, 2021.
- Eric Wan and Alex Nelson. Dual kalman filtering methods for nonlinear prediction, smoothing and estimation. *Advances in neural information processing systems*, 9, 1996.
- Eric A Wan and Alex T Nelson. Dual extended kalman filter methods. *Kalman filtering and neural networks*, pages 123–173, 2001.

- Nicolas Chopin, Pierre E Jacob, and Omiros Papaspiliopoulos. Smc2: an efficient algorithm for sequential analysis of state space models. *Journal of the Royal Statistical Society Series B: Statistical Methodology*, 75(3):397–426, 2013.
- Dan Crisan and Joaquin Miguez. Nested particle filters for online parameter estimation in discrete-time state-space markov models. 2018.
- Adam Paszke, Sam Gross, Francisco Massa, Adam Lerer, James Bradbury, Gregory Chanan, Trevor Killeen, Zeming Lin, Natalia Gimelshein, Luca Antiga, et al. Pytorch: An imperative style, high-performance deep learning library. *Advances in neural information processing systems*, 32, 2019.
- James Bradbury, Roy Frostig, Peter Hawkins, Matthew James Johnson, Chris Leary, Dougal Maclaurin, George Necula, Adam Paszke, Jake VanderPlas, Skye Wanderman-Milne, and Qiao Zhang. JAX: composable transformations of Python+NumPy programs, 2018. URL <http://github.com/google/jax>.
- Adam Paszke, Sam Gross, Soumith Chintala, Gregory Chanan, Edward Yang, Zachary DeVito, Zeming Lin, Alban Desmaison, Luca Antiga, and Adam Lerer. Automatic differentiation in pytorch. 2017.
- Torsten A Enßlin, Mona Frommert, and Francisco S Kitaura. Information field theory for cosmological perturbation reconstruction and nonlinear signal analysis. *Physical Review D*, 80(10):105005, 2009.
- Torsten Enßlin. Information field theory. In *AIP Conference Proceedings*, volume 1553, pages 184–191. American Institute of Physics, 2013.
- Torsten A Enßlin. Information theory for fields. *Annalen der Physik*, 531(3):1800127, 2019.
- Alex Alberts and Ilias Bilionis. Physics-informed information field theory for modeling physical systems with uncertainty quantification. *Journal of Computational Physics*, 486:112100, 2023.
- Philipp Frank, Reimar Leike, and Torsten A Enßlin. Field dynamics inference for local and causal interactions. *Annalen der Physik*, 533(5):2000486, 2021.
- Margret Westerkamp, Igor Ovchinnikov, Philipp Frank, and Torsten Enßlin. Dynamical field inference and supersymmetry. *Entropy*, 23(12):1652, 2021.
- Tom Lancaster and Stephen J Blundell. *Quantum field theory for the gifted amateur*. OUP Oxford, 2014.
- Jakob Knollmüller and Torsten A Enßlin. Metric gaussian variational inference. *arXiv preprint arXiv:1901.11033*, 2019.
- Kairui Hao and Ilias Bilionis. An information field theory approach to bayesian state and parameter estimation in dynamical systems. *Journal of Computational Physics*, page 113139, 2024.
- Richard P Feynman, Albert R Hibbs, and Daniel F Styer. *Quantum mechanics and path integrals*. Courier Corporation, 2010.
- Jean Zinn-Justin. *Quantum field theory and critical phenomena*, volume 171. Oxford university press, 2021.
- Ulf Grenander and Michael I Miller. Representations of knowledge in complex systems. *Journal of the Royal Statistical Society: Series B (Methodological)*, 56(4):549–581, 1994.
- Max Welling and Yee W Teh. Bayesian learning via stochastic gradient langevin dynamics. In *Proceedings of the 28th international conference on machine learning (ICML-11)*, pages 681–688, 2011.
- Matthew D Hoffman, David M Blei, Chong Wang, and John Paisley. Stochastic variational inference. *Journal of Machine Learning Research*, 2013.
- Maziar Raissi, Paris Perdikaris, and George E Karniadakis. Physics-informed neural networks: A deep learning framework for solving forward and inverse problems involving nonlinear partial differential equations. *Journal of Computational physics*, 378:686–707, 2019.
- Kaiming He, Xiangyu Zhang, Shaoqing Ren, and Jian Sun. Deep residual learning for image recognition. In *Proceedings of the IEEE conference on computer vision and pattern recognition*, pages 770–778, 2016.
- Matthew Tancik, Pratul Srinivasan, Ben Mildenhall, Sara Fridovich-Keil, Nithin Raghavan, Utkarsh Singhal, Ravi Ramamoorthi, Jonathan Barron, and Ren Ng. Fourier features let networks learn high frequency functions in low dimensional domains. *Advances in Neural Information Processing Systems*, 33:7537–7547, 2020.
- Oliver Hennigh, Susheela Narasimhan, Mohammad Amin Nabian, Akshay Subramaniam, Kaustubh Tangsali, Zhiwei Fang, Max Rietmann, Wonmin Byeon, and Sanjay Choudhry. Nvidia simnet™: An ai-accelerated multi-physics simulation framework. In *International conference on computational science*, pages 447–461. Springer, 2021.
- James D Meiss. *Differential dynamical systems*. SIAM, 2007.
- Neal Parikh, Stephen Boyd, et al. Proximal algorithms. *Foundations and trends® in Optimization*, 1(3):127–239, 2014.

- Nasim Rahaman, Aristide Baratin, Devansh Arpit, Felix Draxler, Min Lin, Fred Hamprecht, Yoshua Bengio, and Aaron Courville. On the spectral bias of neural networks. In *International Conference on Machine Learning*, pages 5301–5310. PMLR, 2019.
- Sifan Wang, Xinling Yu, and Paris Perdikaris. When and why pinns fail to train: A neural tangent kernel perspective. *Journal of Computational Physics*, 449:110768, 2022.
- Solomon Kullback and Richard A Leibler. On information and sufficiency. *The annals of mathematical statistics*, 22(1): 79–86, 1951.
- Michael I Jordan, Zoubin Ghahramani, Tommi S Jaakkola, and Lawrence K Saul. An introduction to variational methods for graphical models. *Machine learning*, 37:183–233, 1999.
- Diederik P Kingma and Max Welling. Auto-encoding variational bayes. *arXiv preprint arXiv:1312.6114*, 2013.
- Paul Langevin. Sur la théorie du mouvement brownien. *Compt. Rendus*, 146:530–533, 1908.
- Herbert Robbins and Sutton Monro. A stochastic approximation method. *The annals of mathematical statistics*, pages 400–407, 1951.
- Sam Patterson and Yee Whye Teh. Stochastic gradient riemannian langevin dynamics on the probability simplex. *Advances in neural information processing systems*, 26, 2013.
- Chunyu Li, Changyou Chen, David Carlson, and Lawrence Carin. Preconditioned stochastic gradient langevin dynamics for deep neural networks. In *Proceedings of the AAAI conference on artificial intelligence*, volume 30, 2016.
- Geoffrey Hinton, Nitish Srivastava, and Kevin Swersky. Neural networks for machine learning lecture 6a overview of mini-batch gradient descent. *Cited on*, 14(8):2, 2012.
- Fan Kong, Renjie Han, Shujin Li, and Wei He. Non-stationary approximate response of non-linear multi-degree-of-freedom systems subjected to combined periodic and stochastic excitation. *Mechanical Systems and Signal Processing*, 166:108420, 2022.
- William H Press. *Numerical recipes 3rd edition: The art of scientific computing*. Cambridge university press, 2007.
- Diederik P Kingma and Jimmy Ba. Adam: A method for stochastic optimization. *arXiv preprint arXiv:1412.6980*, 2014.
- Prajit Ramachandran, Barret Zoph, and Quoc V Le. Searching for activation functions. *arXiv preprint arXiv:1710.05941*, 2017.
- Tianzhi Li, Claudio Sbarufatti, and Francesco Cadini. Multiple local particle filter for high-dimensional system identification. *Mechanical Systems and Signal Processing*, 209:111060, 2024.
- Christian E Silva, Amin Maghareh, Hongcheng Tao, Shirley J Dyke, and James Gibert. Evaluation of energy and power flow in a nonlinear energy sink attached to a linear primary oscillator. *Journal of Vibration and Acoustics*, 141(6): 061012, 2019.
- K Worden. Data processing and experiment design for the restoring force surface method, part i: integration and differentiation of measured time data. *Mechanical Systems and Signal Processing*, 4(4):295–319, 1990.
- Izrail Moiseevich Gel'fand and N Ya Vilenkin. *Generalized functions: Applications of harmonic analysis*, volume 4. Academic press, 2014.